Cell

A Cellular Mechanism to Detect and Alleviate Reductive Stress

Graphical Abstract

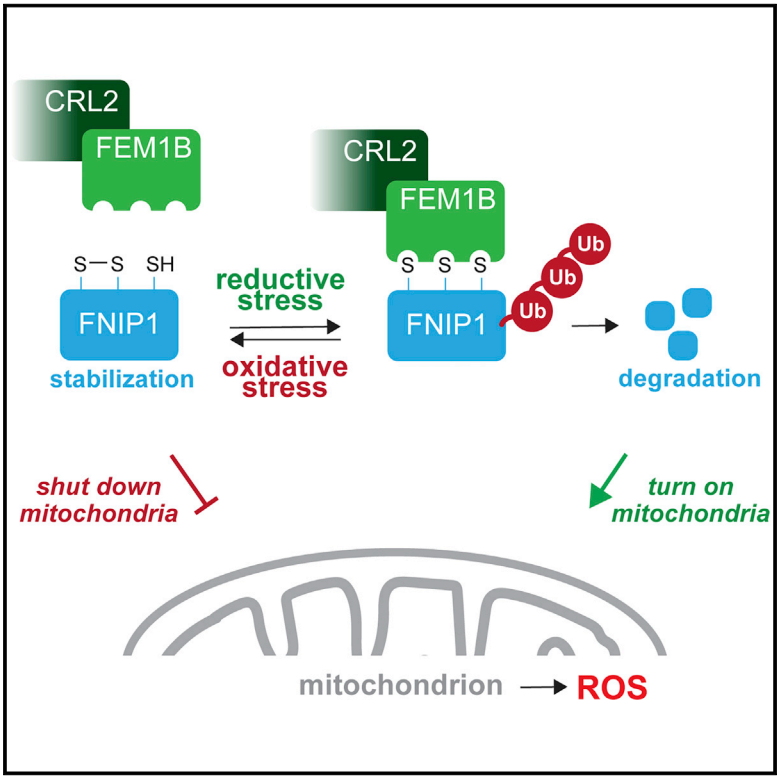

Highlights

- Lack of reactive oxygen species, or reductive stress, prevents myogenesis
- Reductive stress reverses oxidation of invariant Cys residues in FNIP1
- Only reduced, but not oxidized, FNIP1 is polyubiquitylated by $CUL2^{FEM1B}$
- FNIP1 degradation leads to activation of mitochondria to recalibrate ROS

Authors

Andrew G. Manford, Fernando Rodríguez-Pérez, Karen Y. Shih, ..., Denis V. Titov, Daniel K. Nomura, Michael Rape

Correspondence

mrape@berkeley.edu

In Brief

The reductive stress response senses mitochondrial inactivity, as indicated by a drop in reactive oxygen species, and induces proteasomal degradation events that ramp up cellular metabolism to safeguard redox homeostasis and stem cell integrity.

Manford et al., 2020, Cell *183*, 46–61
October 1, 2020
https://doi.org/10.1016/j.cell.2020.08.034

CellPress

CellPress

Cell

Article

A Cellular Mechanism to Detect and Alleviate Reductive Stress

Andrew G. Manford,[1] Fernando Rodríguez-Pérez,[1,2] Karen Y. Shih,[1,2] Zhuo Shi,[1] Charles A. Berdan,[4] Mangyu Choe,[1,4,5] Denis V. Titov,[1,4,5] Daniel K. Nomura,[1,4,6] and Michael Rape[1,2,3,7,*]

[1]Department of Molecular and Cell Biology, University of California at Berkeley, Berkeley CA 94720, USA
[2]Howard Hughes Medical Institute, University of California at Berkeley, Berkeley CA 94720, USA
[3]California Institute for Quantitative Biosciences (QB3), University of California at Berkeley, Berkeley, CA 94720, USA
[4]Department of Nutritional Science and Toxicology, University of California at Berkeley, Berkeley CA 94720, USA
[5]Center for Computational Biology, University of California at Berkeley, Berkeley CA 94720, USA
[6]Department of Chemistry, University of California at Berkeley, CA 94720, USA
[7]Lead Contact
*Correspondence: mrape@berkeley.edu
https://doi.org/10.1016/j.cell.2020.08.034

SUMMARY

Metazoan organisms rely on conserved stress response pathways to alleviate adverse conditions and preserve cellular integrity. Stress responses are particularly important in stem cells that provide lifetime support for tissue formation and repair, but how these protective systems are integrated into developmental programs is poorly understood. Here we used myoblast differentiation to identify the E3 ligase $CUL2^{FEM1B}$ and its substrate FNIP1 as core components of the reductive stress response. Reductive stress, as caused by prolonged antioxidant signaling or mitochondrial inactivity, reverts the oxidation of invariant Cys residues in FNIP1 and allows $CUL2^{FEM1B}$ to recognize its target. The ensuing proteasomal degradation of FNIP1 restores mitochondrial activity to preserve redox homeostasis and stem cell integrity. The reductive stress response is therefore built around a ubiquitin-dependent rheostat that tunes mitochondrial activity to redox needs and implicates metabolic control in coordination of stress and developmental signaling.

INTRODUCTION

Metazoan development relies on carefully balanced transcriptional networks to generate the more than 200 cell types of an adult organism. Stem cells are at the apex of this intricate program, and their defective homeostasis gives rise to many pediatric diseases (Avior et al., 2016; Nusse and Clevers, 2017). Because pluripotent cells also support tissue repair, their aberrant maintenance has been linked to tumorigenesis and tissue degeneration (Almada and Wagers, 2016).

To protect their stem cell populations from damage, organisms possess conserved stress response pathways that detect and alleviate a wide range of adverse conditions. Many stem cells reside in hypoxic niches and rely on glycolysis as a main source of energy, which limits oxidative damage to DNA, lipids, or proteins (Donato et al., 2017; Ezashi et al., 2005; Studer et al., 2000). If too many reactive oxygen species (ROS) accumulate, these cells activate the oxidative stress response to stabilize the transcription factor nuclear factor erythroid 2-related factor 2 (NRF2). NRF2 drives expression of proteins that scavenge oxidizing molecules and revert oxidized proteins into their functional reduced state (Suzuki and Yamamoto, 2017). Failure to elicit antioxidant signaling impairs stem cell self-renewal and differentiation and endangers tissue maintenance (Tsai et al., 2013; Yamamoto et al., 2018). Stem cell integrity is similarly preserved by stress responses that are activated by protein misfolding, DNA damage, or lack of oxygen (Balchin et al., 2016; Ohh et al., 2000; Vilchez et al., 2014).

Mirroring their rapid activation, stress responses have to be shut off soon after cellular homeostasis has been restored. Stem cells that do not turn off the oxidative stress response fail to accumulate physiological ROS required for signaling and are unable to differentiate (Bellezza et al., 2018; Gores et al., 1989; Holmström and Finkel, 2014; Rodríguez-Colman et al., 2017; Sena and Chandel, 2012; Xiao and Loscalzo, 2020). A persistent lack of ROS, or reductive stress, also impedes insulin signaling and glucose homeostasis (McClung et al., 2004); blunts positive effects of exercise on insulin sensitivity (Ristow et al., 2009); triggers cardiomyopathy, obesity, or diabetes (Dialynas et al., 2015; McClung et al., 2004; Rajasekaran et al., 2007, 2011; Wu et al., 2016); and increases mortality (Bjelakovic et al., 2007). Despite such dire consequences, how reductive stress is sensed and alleviated is still unknown.

Stress responses are often controlled by ubiquitylation, a modification whose specificity is imparted by hundreds of E3 ligases (Balchin et al., 2016; Buckley et al., 2012; Oh et al., 2018; Rape, 2018; Yau and Rape, 2016). Kelch-like erythroid cell-derived protein with CNC homology-associated protein 1 (KEAP1) pairs up

with Cullin-3 (CUL3) and RBX1 to form the E3 $CUL3^{KEAP1}$, which sequesters and ubiquitylates NRF2 (Wakabayashi et al., 2003). When cells experience oxidative stress, $CUL3^{KEAP1}$ is inhibited, and NRF2 accumulates in the nucleus to drive antioxidant gene expression (Furukawa and Xiong, 2005; Itoh et al., 2003; Zhang et al., 2004). The E3 $CUL2^{VHL}$ similarly restricts HIF-1α until hypoxic stress stabilizes this transcription factor to initiate angiogenesis (Denko, 2008; Kaelin, 2007). Underscoring the importance of accurate stress signaling, deletion of *VHL* or *KEAP1* elicits embryonic or early postnatal death, respectively (Gnarra et al., 1997; Wakabayashi et al., 2003), and their mutation is a frequent cause of cancer (Cancer Genome Atlas Research Network, 2012; Kaelin, 2007). Whether reductive stress is also controlled by a ubiquitin-dependent stress response and whether this is important for development has not been investigated.

Here we made use of the redox-sensitive pathways underlying myoblast differentiation to identify $CUL2^{FEM1B}$ and its target Folliculin-interacting protein 1 (FNIP1) as core components of the reductive stress response. Reductive stress as a consequence of persistent mitochondrial inactivity or antioxidant signaling reverses oxidation of invariant Cys residues in FNIP1, a prerequisite for $CUL2^{FEM1B}$ to bind its substrate. The ensuing ubiquitylation and proteasomal degradation of FNIP1 increase mitochondrial output to generate ROS and preserve redox homeostasis. The reductive stress response is therefore built around a ubiquitin-dependent rheostat that tunes mitochondrial output to cellular needs and couples stress and developmental signaling in vertebrates.

RESULTS

Reductive Stress Inhibits Myoblast Differentiation

As a tissue reliant on oxygen consumption, muscle provides a system to identify proteins with roles in redox stress management (Almada and Wagers, 2016; Braun and Gautel, 2011). This prompted us to ask whether Cullin-Ring-E3 ligases (CRLs), a family of E3s known to control stress and developmental signaling (Bellezza et al., 2018; Donato et al., 2017; Lignitto et al., 2019; Ohh et al., 2000; Wang et al., 1999; Werner et al., 2015), are required for myogenesis *in vitro*. We depleted each of seven Cullin scaffolds from C2C12 myoblasts and followed myotube formation by staining for myosin heavy chain (MyHC) (Bader et al., 1982). These experiments showed that CUL2 and CUL3 were particularly important for myotube formation (Figure S1A), which is consistent with the effects of *CUL3* deletion on muscle development in mice (Blondelle et al., 2017; Papizan et al., 2018).

CUL2 and CUL3 select their substrates through adaptors containing VHL boxes or BTB domains (Silverman et al., 2012; Skaar et al., 2013). Using affinity purification of CUL2 and CUL3 coupled to mass spectrometry, we detected 19 CUL2 and 32 CUL3 adaptors in myoblasts or myotubes (Table S1). This included candidate adaptors, such as the muscular dystrophy protein myoferlin, and factors linked to familial myopathy, such as KLHL9. After combining this list with adaptors from other cell types (Bennett et al., 2010; Mahrour et al., 2008; Mena et al., 2018), we depleted 156 CRL2 and CRL3 subunits from myoblasts, initiated differentiation, and recorded MyHC-positive myotubes by microscopy and automated image analysis (Figure 1A). Critical phenotypes were confirmed with multiple small interfering RNAs (siRNAs) to eliminate the risk of off-target effects.

Our screen revealed that the CUL3 adaptors KEAP1, BTBD9, KLHL22, and ANKFY1 were required for myotube formation, whereas depletion of the CUL2 adaptor fem-1 homolog B (FEM1B) strongly improved this differentiation program (Figures 1A–1C). Because loss of these adaptors minimally affected cell numbers (Figure S1B), aberrant cell division or survival was unlikely to account for the changes in cell fate specification. Notably, all adaptors required for myotube formation had links to disease; mutations in *KEAP1* lead to lung and renal cancer (Kovac et al., 2015; Singh et al., 2006), *BTBD9* mutations trigger restless leg syndrome and insomnia (Winkelmann et al., 2007), KLHL22 overexpression causes breast cancer progression (Chen et al., 2018), and mutations in *ANKFY1* result in steroid-resistant nephrotic syndrome (Hermle et al., 2018).

We were intrigued to see that depletion of the oxidative stress sensor KEAP1 prevented myoblast differentiation. Although oxidative stress transiently inhibits $CUL3^{KEAP1}$ (Zhang et al., 2004), genetic loss of KEAP1 stabilizes NRF2 for prolonged periods of time and elicits reductive stress (Rajasekaran et al., 2011). KEAP1 depletion in myoblasts induced accumulation of NRF2 (Figures 1C and 1D) and its target genes (Figures 2E and 2F). This caused an increase in NADPH levels (Figure S1C) and a steep drop in ROS, the hallmark of reductive stress (Figure 1E). When we blunted such antioxidant signaling by co-depleting NRF2 or enzymes of glutathione synthesis and recycling, differentiation was restored (Figures 1D and 1F; Figure S1D). Scavengers of mitochondrion-derived ROS, which impose reductive stress by chemical means (Banba et al., 2019; Brand et al., 2016; Orr et al., 2015), also inhibited myoblast differentiation (Figure 1G). We therefore conclude that, consistent with recent findings using KEAP1 inhibitors (Rajasekaran et al., 2020), reductive stress impairs myogenesis *in vitro*. Although this lent support to the notion that ROS fulfill critical signaling roles (Holmström and Finkel, 2014; Sena and Chandel, 2012), it reinforced the question of how reductive stress is sensed and counteracted during normal development.

FEM1B Counteracts KEAP1

To dissect cellular responses to reductive stress, we designed a genetic modifier screen aimed at rescuing differentiation of KEAP1-deficient myoblasts. Focusing on E3 ligases as likely stress regulators, we found that depletion of the CUL2 adaptor FEM1B enabled myotube formation despite lack of KEAP1 (Figure 2A). We confirmed this result with independent siRNAs in microscopy and western blot analyses of myoblast differentiation (Figures 2B and 2C). Loss of FEM1B also rescued differentiation in the presence of scavengers of mitochondrion-derived ROS, showing that FEM1B affects reductive stress imposed by genetic or chemical means (Figure 2D). Intriguingly, FEM1B had already emerged from our initial screen as hit whose depletion showed the strongest increase in efficiency of myotube formation (Figure 1A), the opposite phenotype of loss of KEAP1.

Gene expression analyses showed that KEAP1 depletion induced antioxidant NRF2 targets, such as enzymes of glutathione synthesis, ROS scavengers, or components of the pentose phosphate pathway (Figures 2E and 2F; Figures S2A

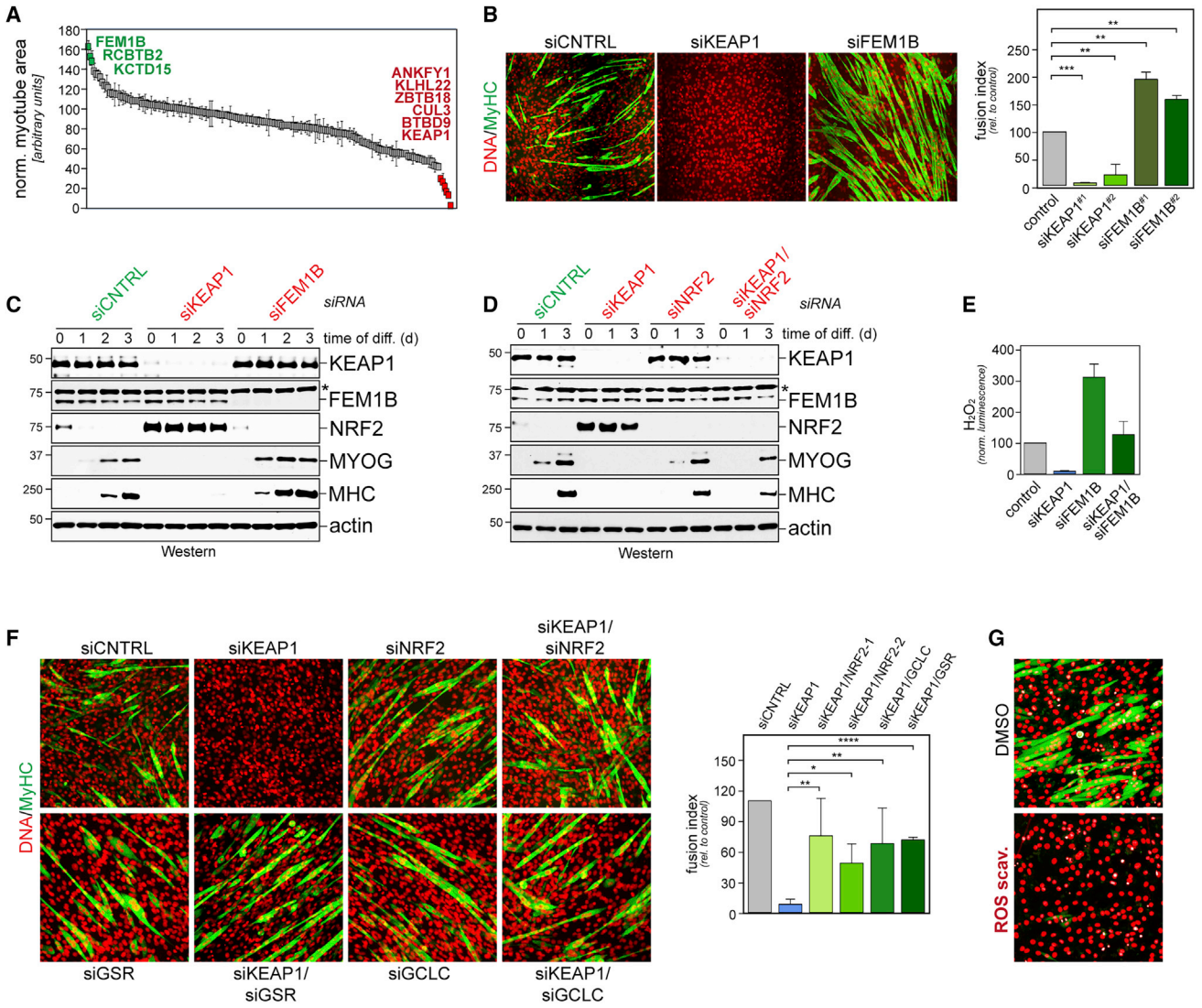

Figure 1. Reductive Stress Inhibits Myotube Formation

(A) C2C12 myoblasts were depleted of each CUL2 and CUL3 substrate adaptor and induced to differentiate. Myotube formation was followed by immunofluorescence analysis against myosin heavy chain (MyHC).

(B) C2C12 myoblasts were depleted of KEAP1 or FEM1B, and myotube formation was determined as above. Right: quantification of at least three biological replicates with mean ± SD.

(C) C2C12 myoblasts were depleted of KEAP1 or FEM1B, and expression of myogenesis markers was determined by western blotting.

(D) C2C12 cells were depleted of KEAP1, NRF2, or both, and differentiation efficiency was monitored by western blotting against MYOG and MyHC.

(E) C2C12 myoblasts were depleted of KEAP1, FEM1B, or both, and cellular H_2O_2 was measured using a luciferase reporter.

(F) C2C12 myoblasts were depleted of KEAP1, NRF2, antioxidant targets of NRF2 (GSR and GCLC), or combinations thereof. The differentiation efficiency of myotube formation was determined by staining for MyHC. Right: quantification of at least three experiments with mean ± SD.

(G) Myogenesis is impaired by mitochondrial complex I and III ROS scavengers. S1QEL1.1 and S3QEL 2 were added during C2C12 myoblast differentiation, which was analyzed as above.

See also Figure S1 and Table S1.

and S2B). Depletion of FEM1B had the opposite effect and reduced NRF2 targets but increased the myogenic markers MYOG and MYL1 (Figures 2E and 2F). Importantly, concomitant depletion of KEAP1 and FEM1B cancelled each of these phenotypes of single E3 ligase depletion (Figures 2E and 2F; Figure S2A). Consistent with these results, depletion of FEM1B restored ROS levels in KEAP1-deficient myoblasts (Figure 1E).

Although KEAP1 is best known for controlling NRF2 levels; it also sequesters the transcription factor in the cytoplasm (Itoh et al., 2003). Although FEM1B depletion reduced NRF2 mRNA (Figure S2C), it had only a minor effect on the abundance of the NRF2 protein (Figure 2C). In contrast, loss of FEM1B had striking effects on NRF2 localization; although NRF2 accumulated in the nucleus of KEAP1-deficient myoblasts, co-depletion

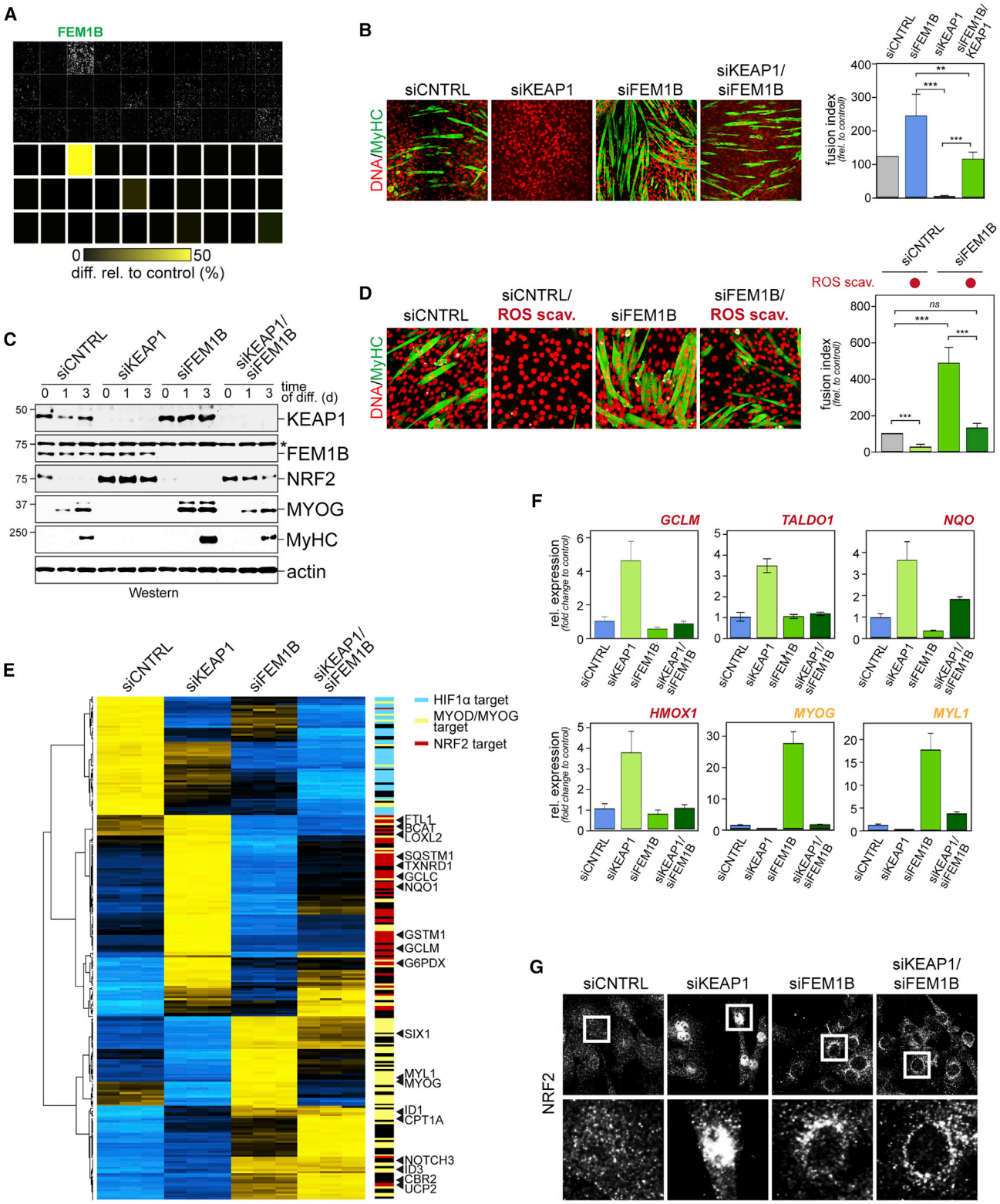

Figure 2. Depletion of FEM1B Enables Myoblast Differentiation Despite Reductive Stress

(A) C2C12 myoblasts were depleted in duplicate of KEAP1 and CUL2 adaptors, and differentiation was monitored by microscopy against MyHC. Top panel: microscopy images from each condition. Bottom panel: quantification of differentiation efficiency compared with KEAP1-depleted control cells.

(legend continued on next page)

of FEM1B directed NRF2 to perinuclear regions, where it cannot induce gene expression (Figure 2G). Our results therefore identified FEM1B as a critical regulator of redox signaling and raised the possibility that the E3 $CUL2^{FEM1B}$ might affect, directly or indirectly, the reductive stress response.

$CUL2^{FEM1B}$ Targets FNIP1 for Proteasomal Degradation

Previous work denoted a Leu residue in the VHL box of CUL2 adaptors that engages a pocket on Elongin C to connect the adaptor to the catalytic module also composed of CUL2, Elongin B, and RBX1 (Bullock et al., 2006; Mahrour et al., 2008; Stebbins et al., 1999). Mutation of the respective FEM1B residue, Leu597, produced an adaptor that failed to bind CUL2 and, hence, cannot support ubiquitylation (Figure S2D) but contained ankyrin repeats and should thus retain its ability to recognize substrates. As seen with other CRLs (Mena et al., 2018), we expected $FEM1B^{L597A}$ to show prolonged binding to otherwise short-lived targets to facilitate their identification by CompPASS mass spectrometry (Huttlin et al., 2017).

Proteomics analyses confirmed that $FEM1B^{L597A}$ was impaired in binding to CUL2, Elongin B, and Elongin C (Figure 3A). In contrast, $FEM1B^{L597A}$ interacted more strongly than FEM1B with several proteins considered to be candidate substrates. These included the GATOR1 complex, which inhibits mTORC1 signaling during amino acid limitation (Bar-Peled et al., 2013; Dutchak et al., 2018), as well as Folliculin (FLCN) and FNIP1, which also bind each other (Baba et al., 2006). A close FNIP1 homolog, FNIP2, was not detected. We confirmed, by immunoprecipitation and western blotting, that FEM1B associated with GATOR1, FLCN, and FNIP1 in a manner that was stabilized by mutation of the VHL box in FEM1B (Figure 3B; Figure S2E). In contrast, mutation of Cys186, an invariant residue in the substrate-binding ankyrin repeats, strongly diminished recognition of GATOR1, FLCN, and FNIP1 by FEM1B (Figure 3B).

FEM1B overexpression elicited CUL2- and proteasome-dependent degradation of FNIP1, whereas substrate binding-deficient $FEM1B^{C186S}$, inactive $FEM1B^{L597A}$, or the related adaptor FEM1A did not have this effect (Figure 3C; Figures S2E and S2F). Depletion of FEM1B caused the opposite outcome and increased levels of endogenous FNIP1 (Figure 3D). NEDD8-modified $CUL2^{FEM1B}$ also polyubiquitylated FNIP1 *in vitro* when incubated with the E2 enzymes UBE2D3 and UBE2R1 (Figure 3E). In contrast, expression of FEM1B did not induce degradation of FLCN, GATOR1 subunits, or FNIP2 (Figure 3B; Figures S2E–S2G), and $CUL2^{FEM1B}$ did not ubiquitylate these proteins *in vitro* (Figure 3E; Figure S2H). We conclude that FNIP1 is a proteolytic $CUL2^{FEM1B}$ substrate, whereas FLCN or GATOR1 might interact with FEM1B indirectly or in a role that is distinct from being a degradation target.

Although loss of FNIP1 had little effect on differentiation (Figure S2I), FNIP1, but not GATOR1, co-depletion reverted the effects of FEM1B loss on myotube formation (Figure 3F; Figures S2I and S2J). Thus, accumulation of FNIP1 promoted differentiation in the absence of FEM1B. Loss of FNIP1 also prevented myogenesis in cells lacking both FEM1B and KEAP1 (Figure 3G) and caused NRF2 to re-enter the nucleus (Figure 3H), which documents that it was FNIP1 stabilization that allowed myoblasts to bypass reductive stress.

We conclude that FNIP1 is a critical target of $CUL2^{FEM1B}$ during reductive stress. Previous work implicated FNIP1 in mitochondrial biogenesis (Hasumi et al., 2012; Reyes et al., 2015), removal of damaged mitochondria (Heo et al., 2018), and regulation of the AMPK and mTORC1 kinases (Baba et al., 2006; Bhargava and Schnellmann, 2017; Hasumi et al., 2008; Tsun et al., 2013). Although somatic *FNIP1* variants have been detected in renal cancer (Cancer Genome Atlas Research Network, 2013), mutations in its partner FLCN cause Birt-Hogg-Dubé syndrome (Nickerson et al., 2002), a predisposition to renal cancer that also results from aberrant mitochondrial activity or mutations in *VHL*, *KEAP1*, or *NFE2L2* (Kaelin, 2007; Kovac et al., 2015; Xu et al., 2019).

FEM1B Detects a Conserved Cys Degron in FNIP1

To determine whether ROS modulates recognition of FNIP1 by $CUL2^{FEM1B}$, we first needed to identify the FNIP1 degron that is bound by FEM1B. Through deletion analyses, we found a short stretch in the central region of FNIP1 that was required for recognition by $CUL2^{FEM1B}$ and its proteasomal degradation (Figures 4A and 4B). As expected for a transferable motif, a degron fusion to GFP (GFP^{degron}) was readily detected by $CUL2^{FEM1B}$ (Figures S3A and S3B). As with full-length FNIP1, GFP^{degron} showed stronger binding to the substrate trap $FEM1B^{L597A}$ (Figure S3A), but it did not interact with $FEM1B^{C186S}$ (Figure S3B). We next expressed GFP^{degron} along with mCherry and used the GFP/mCherry ratio as a quantitative readout for protein degradation. FEM1B, but not $FEM1B^{L597A}$ or $FEM1B^{C186S}$, triggered dramatic loss of GFP^{degron} (Figure 4C), whereas deletion of *FEM1B* by CRISPR-Cas9, depletion of FEM1B by shRNAs, or proteasome inhibition protected GFP^{degron} from degradation (Figure 4D; Figures S3C and S3D). The FNIP1 degron also mediated a robust interaction with recombinant FEM1B as well as ubiquitylation by $CUL2^{FEM1B}$ (Figures 4E and 4F). A central degron is therefore required and sufficient for FNIP1 ubiquitylation and degradation through $CUL2^{FEM1B}$. Although this degron is conserved among

(B) C2C12 cells were depleted of KEAP1, FEM1B, or both, and differentiation was analyzed by microscopy against MyHC. Right: quantification of four biological replicates with mean ± SD.
(C) C2C12 cells were depleted of KEAP1, FEM1B, or both, and differentiation was analyzed by western blotting.
(D) C2C12 myoblasts depleted of FEM1B were treated throughout differentiation with the ROS scavengers S1QEL1.1 and S3QEL2. Right: quantification of three biological replicates with mean ± SD.
(E) C2C12 myoblasts were depleted of KEAP1, FEM1B, or both. mRNA abundance was measured by RNA sequencing (RNA-seq) and analyzed by unsupervised clustering. Genes with transcription factor binding sites are marked in light blue (HIF1α), green (MYOD/MYOG), or red (NRF2).
(F) qRT-PCR analysis of NRF2 target genes (red) or myogenesis markers (orange) in C2C12 myoblasts depleted of KEAP1, FEM1B, or both. Quantification of three technical replicates ± SD.
(G) NRF2 localization was determined by immunofluorescence in C2C12 myoblasts depleted of KEAP1, FEM1B, or both.
See also Figure S2.

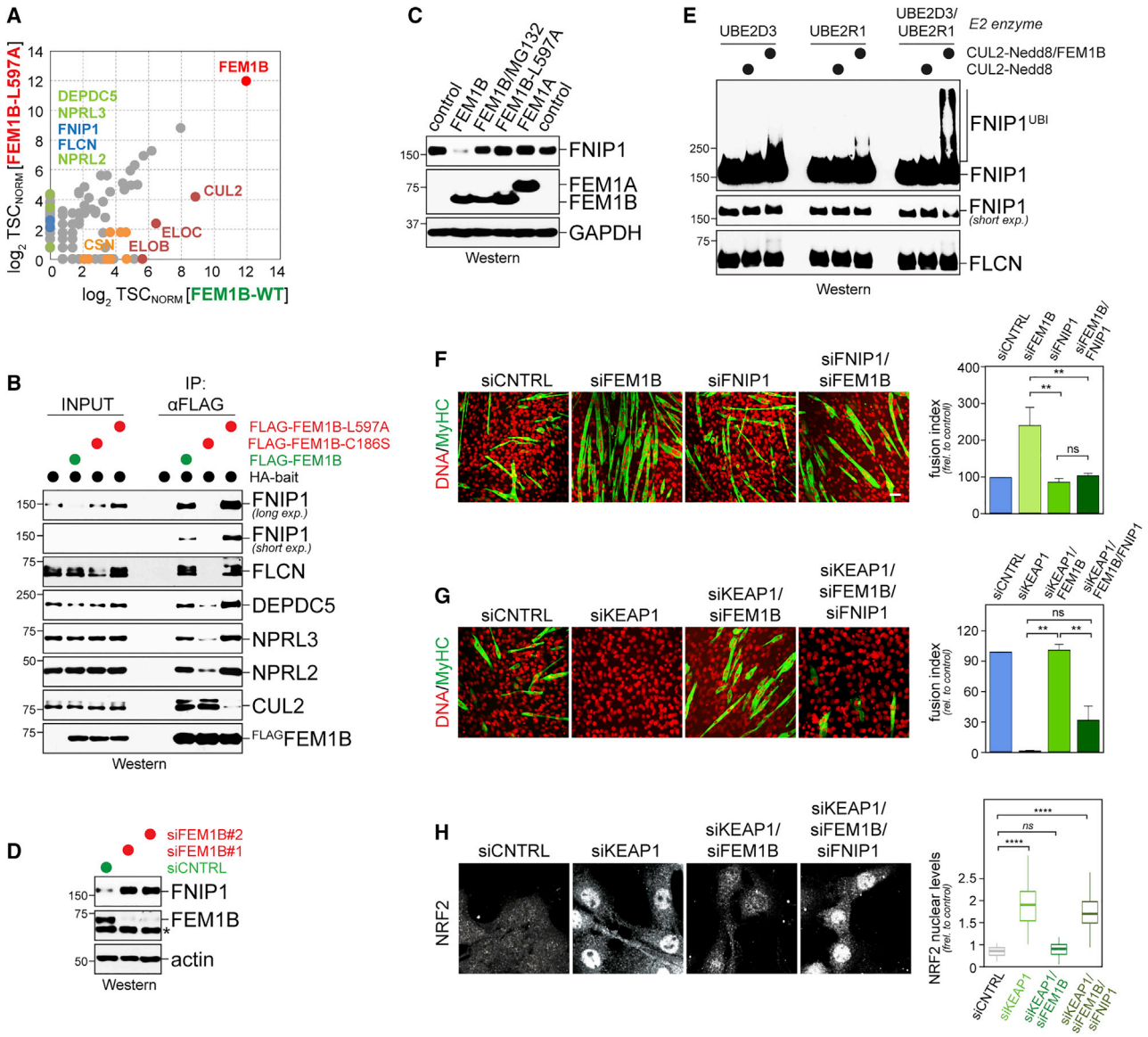

Figure 3. FNIP1 Is a Critical CUL2^{FEM1B} Substrate during Reductive Stress

(A) ^{FLAG}FEM1B or ^{FLAG}FEM1B^{L597A} was purified from C2C12 myoblasts, and binding partners were determined by mass spectrometry. Green, GATOR1; blue, FLCN-FNIP1.

(B) ^{FLAG}FEM1B, ^{FLAG}FEM1B^{C186S}, or ^{FLAG}FEM1B^{L597A} was purified from 293T cells that expressed hemagglutinin (HA)-tagged GATOR1 or FNIP1-FLCN subunits. Co-purifying proteins were detected by αHA-western blotting.

(C) 293T cells were transfected with FEM1B, FEM1B^{L597A}, or FEM1A. The proteasome inhibitor MG132 was added, and endogenous FNIP1 levels were determined by western blotting.

(D) Depletion of FEM1B in 293T cells results in accumulation of endogenous FNIP1, as determined by western blotting.

(E) Ubiquitylation of FNIP1-FLCN by Nedd8-modified CUL2^{FEM1B}, E1, and UBE2D3 and/or UBE2R1 was analyzed by western blotting against FNIP1 (FLAG) and FLCN (HA).

(F) C2C12 myoblasts were depleted of FEM1B, FNIP1, or both, and the efficiency of myotube formation was analyzed by microscopy against MyHC. Right: quantification of at least three biological replicates with mean ± SD.

(G) C2C12 myoblasts were depleted of KEAP1, FEM1B, FNIP1, or combinations thereof, and the efficiency of myotube formation was determined by microscopy against MyHC. Right: quantification of three biological replicates with mean ± SD.

(H) Depletion of FNIP1 allows endogenous NRF2 to enter the nucleus of cells lacking KEAP1 and FEM1B, as determined by immunofluorescence microscopy. Quantification of 15–20 cells/condition ± SD.

See also Figure S3.

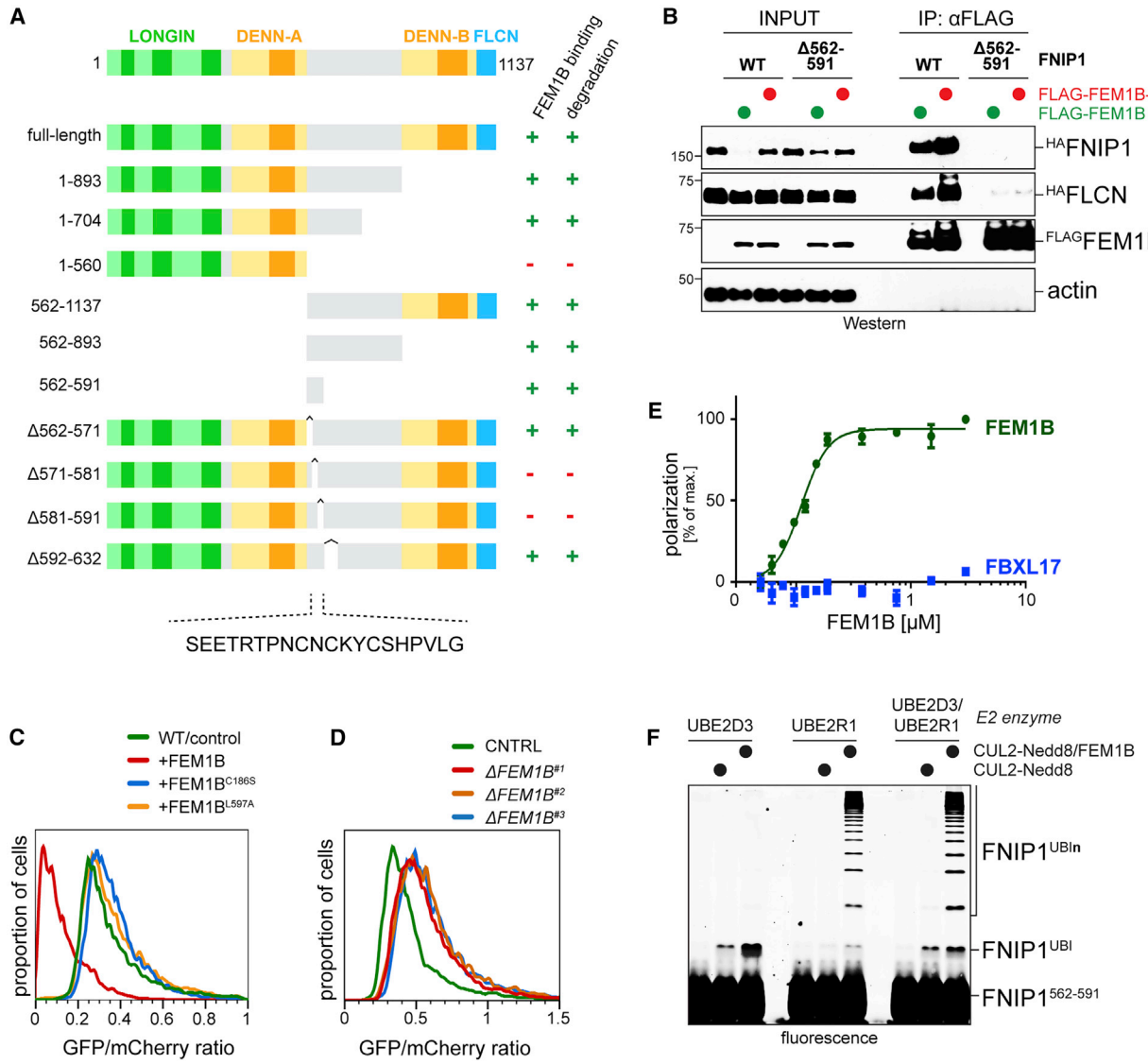

Figure 4. FEM1B Binds a Conserved Degron in FNIP1

(A) FNIP1 variants were tested for interaction with ^{FLAG}FEM1B by co-immunoprecipitation and for degradation by measuring their abundance in the presence or absence of FEM1B.

(B) Wild-type FNIP1 or a variant lacking its degron (FNIP1$^{\Delta 562–591}$) were co-expressed with FLCN and ^{FLAG}FEM1B or ^{FLAG}FEM1B^{L597A}. FEM1B was affinity purified, and bound FNIP1 and FLCN were detected by western blotting.

(C) The FNIP1 degron was fused to GFP (GFP^{degron}) and expressed with mCherry. Cells were transfected with FEM1B, FEM1B^{L597A}, or FEM1B^{C186S}. The ratio of GFP^{degron} to mCherry fluorescence was determined by flow cytometry.

(D) The *FEM1B* locus was deleted in 293T cells using CRISPR-Cas9, and GFP^{degron} degradation was analyzed by flow cytometry.

(E) Binding of a TAMRA-labeled FNIP1 degron peptide to recombinant FEM1B (green) or FBXL17 (blue) was measured by fluorescence polarization with mean ± SD.

(F) Ubiquitylation of a TAMRA-labeled FNIP1 degron by Nedd8-modified CUL2^{FEM1B}, E1, UBE2D3, and/or UBE2R1 was monitored by gel electrophoresis and fluorescence detection.

See also Figure S4.

FNIP1 homologs (Figure S3E), it is not found in the closely related FNIP2, which is not recognized by CUL2^{FEM1B} (Figure S3F).

Given the role of CUL2^{FEM1B} in reductive stress signaling, we were excited to see that the FNIP1 degron contained three invariant Cys residues (Figure S3E). Cys585 was essential for FEM1B-dependent degradation of GFP^{degron} (Figure 5A). Simultaneous mutation of Cys580 and Cys582 strongly impaired clearance of GFP^{degron}, and mutation of all Cys residues fully protected the reporter against CUL2^{FEM1B}-dependent degradation (Figure 5A). Mutating its Cys residues blocked binding of the degron to recombinant FEM1B (Figure 5B) and prevented its ubiquitylation by CUL2^{FEM1B} (Figure 5C). The reliance on Cys

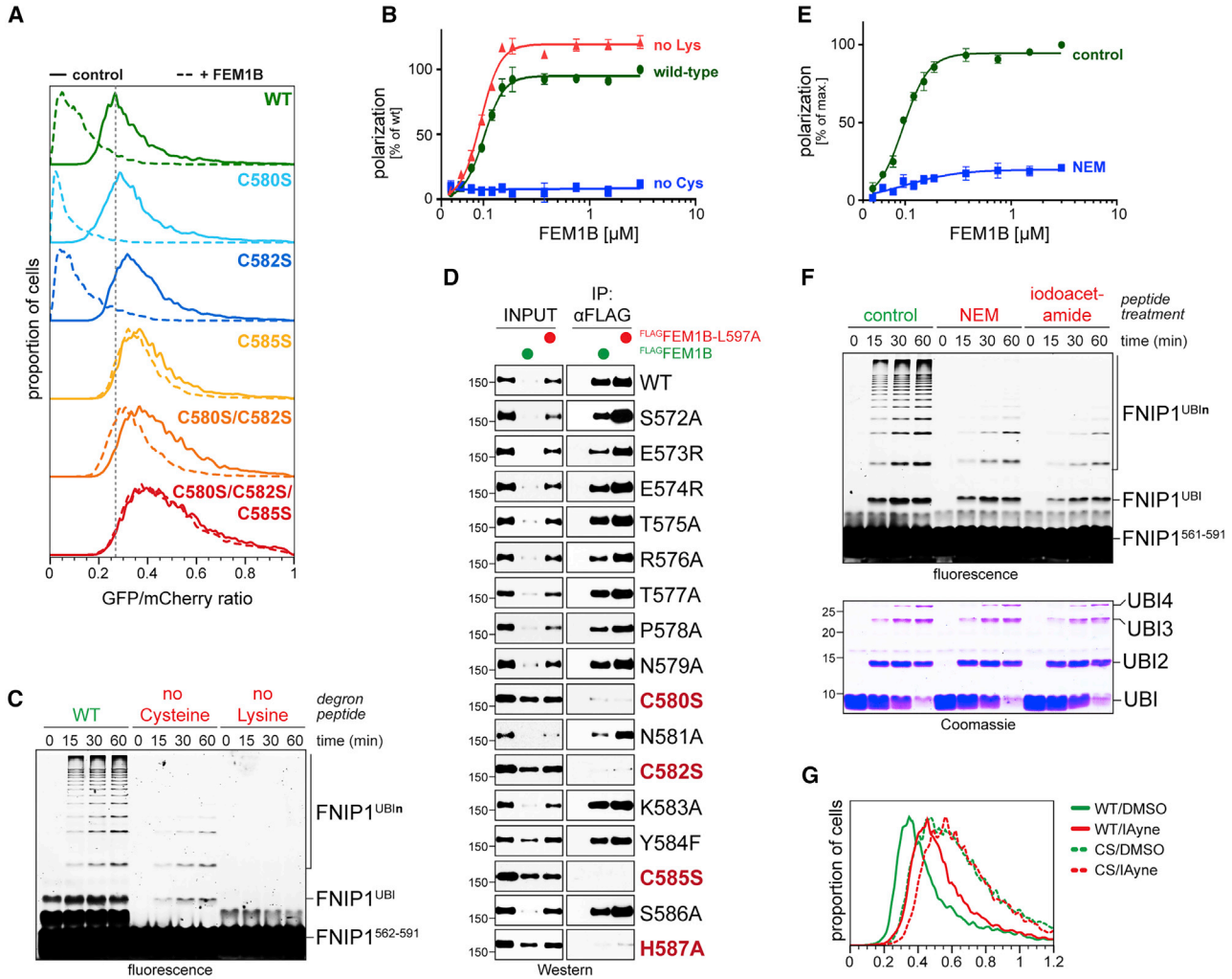

Figure 5. The FNIP1 Degron Requires Cys Residues

(A) GFP^{degron} fusions were expressed with mCherry and FEM1B (dashed lines) or not (solid lines), and the GFP/mCherry ratio was determined by flow cytometry.

(B) Binding of TAMRA-labeled wild-type, Cys-free, or Lys-free degrons to recombinant FEM1B was monitored by fluorescence polarization with mean ± SD.

(C) Ubiquitylation of TAMRA-labeled FNIP1 degrons by Nedd8-modified CUL2^{FEM1B}, E1, and UBE2D3/UBE1R1 was followed by gel electrophoresis and fluorescence imaging.

(D) Levels of ^{HA}FNIP1 variants in cells expressing ^{FLAG}FEM1B or ^{FLAG}FEM1B^{L597A} were monitored by western blotting. E3 binding was determined by FEM1B affinity purification and α^{HA}FNIP1 western blotting.

(E) The TAMRA-labeled FNIP1 degron was incubated in buffer or NEM. The reactions were quenched, and FEM1B binding was monitored by fluorescence polarization with mean ± SD.

(F) The TAMRA-labeled FNIP1 degron was incubated in buffer, NEM, or iodoacetamide. Following quenching, ubiquitylation by Nedd8-modified CUL2^{FEM1B}, E1, and UBE2D3/UBE2R1 was followed by gel electrophoresis and fluorescence imaging or Coomassie staining.

(G) The Cys-reactive, cell-permeable IA-Alkyne stabilizes GFP^{degron} in cells, as seen by flow cytometry.

See also Figure S5.

residues was even more pronounced in full-length FNIP1, where each of the three Cys as well as a neighboring His residue were required for FEM1B binding and proteasomal degradation (Figure 5D; Figure S4A).

In line with this mutational analysis, treatment of the FNIP1 degron with Cys-modifying iodoacetamide or N-ethylmaleimide inhibited its recognition by FEM1B (Figure 5E; Figures S4B and S4C) and its CUL2^{FEM1B}-dependent ubiquitylation (Figure 5F). Similar observations were made in cells, where the iodoacetamide derivative IA-Alkyne impaired FEM1B-dependent degradation of GFP^{degron} (Figure 5G). We conclude that the reductive stress E3 ligase CUL2^{FEM1B} relies on an unmodified Cys degron to detect its essential substrate FNIP1.

Reductive Stress Triggers Detection of FNIP1 by CUL2^{FEM1B}

Given the role of Cys residues in CUL2^{FEM1B} recognition, we next determined the oxidation state of the FNIP1 degron during

normal conditions and reductive stress. Despite treating FNIP1 immunoprecipitates with multiple proteases or even using synthesized peptides, we could not detect the entire degron by proteomic means. This peptide was also absent from global analyses of Cys oxidation, suggesting that it evades analysis by mass spectrometry (Leichert et al., 2008; Souza et al., 2018; van der Reest et al., 2018). Selective derivatization was hampered by 30 additional Cys residues in FNIP1. However, because the degron was prone to disulfide bond formation (Figure S5A), we could analyze its oxidation using the thioredoxin TRX (Lindahl and Florencio, 2003). TRX contains an active site Cys residue that attacks intracellular disulfide bonds before a second TRX Cys targets the mixed disulfide to release a reduced protein. A TRX^{C35S} variant lacking the second Cys fails to resolve the mixed disulfide and covalently traps oxidized proteins; the more a protein is trapped by TRX^{C35S}, the more it is oxidized in cells.

Revealing significant degron oxidation under normal conditions, we found that GFP^{degron}, but not the Cys-free reporter, was efficiently trapped by TRX^{C35S} (Figure 6A). Treatment with α-ketoglutarate, which escalates ROS by increasing flux through the mitochondrial TCA cycle, or antimycin A, which elevates ROS by inhibiting mitochondrial complex III, enhanced TRX^{C35S} trapping of GFP^{degron} or full-length FNIP1 (Figure 6B; Figure S5B). Importantly, ROS depletion after $CUL3^{KEAP1}$ inhibition shielded the degron from TRX^{C35S}, which documented a reversal of degron oxidation during reductive stress (Figure 6C).

Several observations showed that degron oxidation controls FNIP1 recognition by $CUL2^{FEM1B}$. Even brief incubation of the degron without a reducing agent disrupted its binding to FEM1B, which was restored by Tris(2-carboxyethyl)phosphine hydrochloride (TCEP) (Figure 6D). In cells, treatment with α-ketoglutarate or antimycin A stabilized GFP^{degron} (Figures 6E and 6F; Figure S5C), dependent on ROS produced by the respiratory chain (Figure S5C). Similar observations were made for myxothiazol, which increased ROS and stabilized GFP^{degron} (Figures S5D and S5E), and for loss of the antioxidant enzymes GSR and TXRND1 (Figure S5F). Conversely, conditions that evoked reductive stress, as mitochondrial inactivation through glutamine starvation or $CUL3^{KEAP1}$ inhibition, accelerated GFP^{degron} turnover (Figure 6F; Figure S5G).

Extending these results to full-length proteins, antimycin A reduced binding of FNIP1 to FEM1B, but reductive stress strongly promoted this interaction (Figure 6G). In fact, when FEM1B and FNIP1 were present at endogenous levels, we could detect their association only after reductive stress had been imposed by $CUL3^{KEAP1}$ inhibition (Figure 6H). Reductive stress also lowered the protein levels but increased ubiquitylation of endogenous FNIP1 (Figure 6I). We conclude that reductive stress reverses oxidation of Cys residues in the FNIP1 degron and allows $CUL2^{FEM1B}$ to associate with its substrate. These findings identify the FNIP1 degron as a reductive stress sensor that is read out by $CUL2^{FEM1B}$.

FNIP1 Degradation Controls Mitochondrial Function

We speculated that FNIP1 degradation might modulate the activities of AMPK or mTORC1 (Baba et al., 2006, 2012; Hasumi et al., 2012; Tsun et al., 2013) because these kinases control biogenesis of mitochondria, which produce most cellular ROS. However, although loss of FEM1B slightly improved amino acid-dependent activation of mTORC1 in myoblasts, this was stimulated, rather than decreased, by FNIP1 co-depletion (Figure S6A). The minor increase in AMPK activity caused by lack of FEM1B was also unaffected by FNIP1 co-depletion (Figure S6B). Furthermore, mutation of its degron did not affect binding of FNIP1 to AMPK or regulators of mTORC1 (Figure S6C), which indicated that FNIP1 stability did not affect mTORC1 or AMPK signaling in myoblasts.

Alternatively, FNIP1 stability might directly affect mitochondria. Indeed, although FEM1B depletion did not reduce mitochondrial content (Figure S6D), all mitochondria of FEM1B-deficient cells showed a heavily stained matrix in transmission electron microscopy (Figure 7Ab). Mitochondria in FEM1B-depleted cells thus undergo matrix condensation, which been ascribed to a lack of substrate for oxidative phosphorylation (Hackenbrock, 1966). Many mitochondria also displayed onion-like swirling of cristae (Figure 7Ac), indicative of upregulation of respiratory chain components in response to impaired oxidative phosphorylation (Jiang et al., 2017; Walker and Benzer, 2004), and some mitochondria contained large blebs (Figure 7Ad), as observed upon initiation of mitophagy (Jin et al., 2010; Pickles et al., 2018). These phenotypes were rescued by FNIP1 co-depletion (Figure 7Af), showing that FNIP1 stabilization altered mitochondrial morphology, consistent with reduced oxidative phosphorylation.

In line with these findings, FEM1B depletion reduced, but loss of FNIP1 increased, the mitochondrial membrane potential (Figure 7B). Cells lacking FEM1B also contained a fragmented mitochondrial network clustered around the nucleus (Figure 7C) and did not produce mitochondrial ROS (Figure 7D). These phenotypes were rescued by FNIP1 depletion (Figures 7B–7D), showing that FNIP1 stabilization inhibits, but its degradation through $CUL2^{FEM1B}$ increases, mitochondrial output to produce ROS and counteract reductive stress.

FEM1B and FNIP1 Are Metabolic Regulators

How could cytoplasmic FNIP1 degradation improve mitochondrial activity? Mitochondria harbor enzymes for fatty acid β-oxidation and the TCA cycle, which convert acetyl-coenzyme A (CoA) into substrate for oxidative phosphorylation and building blocks for amino acid synthesis. To fuel these reactions, mitochondria import pyruvate, fatty acids, or TCA cycle intermediates, coupling cytoplasmic metabolism with mitochondrial energy production.

We thus wanted to find out whether FNIP1 stability affected glycolysis as a major source of pyruvate. FEM1B depletion reduced the glycolytic rate of myoblasts, whereas the respiratory chain itself was unaffected, as monitored by the oxygen consumption rate (Figures S7A and S7B). The extracellular acidification rate, which reflects secretion of lactate downstream of pyruvate, was also lowered by loss of FEM1B (Figure S7C). Liquid chromatography coupled to mass spectrometry revealed that loss of FEM1B depleted cells of glycolytic and TCA cycle intermediates (Figure 7E; Figure S7D). In addition, lack of FEM1B reduced the levels of glucose (Figure 7E) as well as glucose uptake (Figure S7E). However, only a few glycolytic intermediates increased, and glucose import was only improved mildly, upon

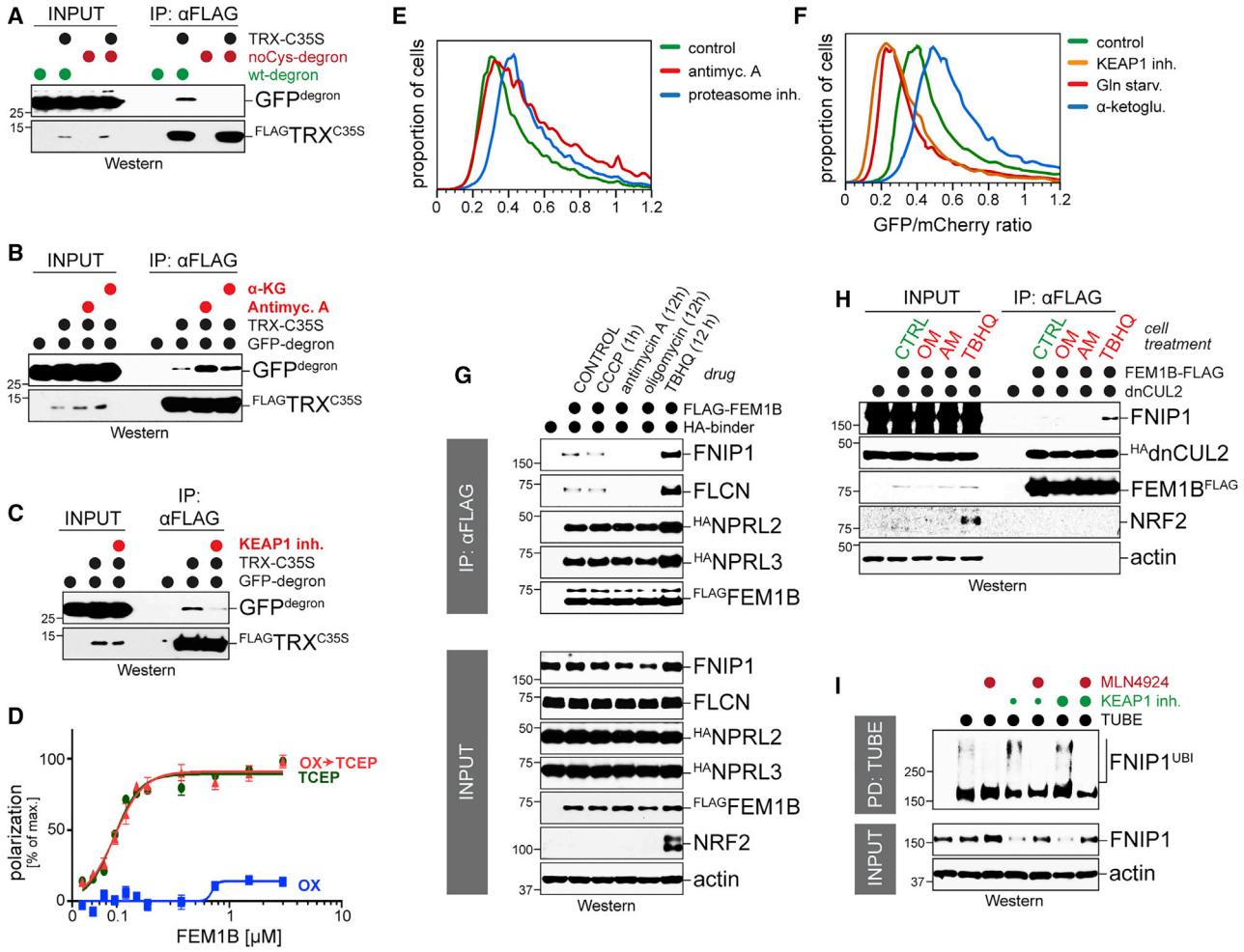

Figure 6. The FNIP1 Degron Is Redox Sensitive

(A) Wild-type or Cys-free GFP^{degron} was tested for TRX^{C35S} trapping, as determined by TRX^{C35S} affinity purification and western blotting against GFP^{degron}.

(B) Cells were treated with cell-permeable α-ketoglutarate or antimycin A, and TRX^{C35S} trapping of GFP^{degron} was determined as above.

(C) TRX^{C35S} trapping of GFP^{degron} was determined in cells treated with the KEAP1 inhibitor bardoxolone.

(D) The TAMRA-labeled FNIP1 degron was diluted in a buffer with (TCEP) or without (OX) reducing agent. After binding to FEM1B was measured by fluorescence polarization, the oxidized degron was treated with TCEP, and binding to FEM1B was monitored again (OX > TCEP) with mean ± SD.

(E) Cells expressing GFP^{degron} were treated with antimycin A or carfilzomib, and the GFP/mCherry ratio was determined by flow cytometry.

(F) Cells expressing GFP^{degron} were exposed to reductive stress by glutamine depletion or KEAP1 inhibition, and the GFP/mCherry ratio was determined by flow cytometry.

(G) ^{FLAG}FEM1B was affinity purified from cells treated with carbonyl cyanide 3-chlorophenylhydrazone (CCCP), antimycin A, oligomycin, or the KEAP inhibitor tert-butylhydroquinone (TBHQ), and binding to endogenous FNIP1 and FLCN or HA-tagged GATOR1 subunits was determined by western blotting.

(H) The *FEM1B* locus of 293T cells was fused to a FLAG epitope. Cells that expressed dominant-negative CUL2 (amino acids 1–427) to stabilize FEM1B-substrate interactions were treated with oligomycin, antimycin A, or TBHQ. Endogenous FEM1B was affinity purified, and bound FNIP1 was detected by western blotting.

(I) 293T cells were treated with bardoxolone with or without the NEDD8 inhibitor MLN4924. Ubiquitylated FNIP1 was isolated using TUBEs and detected by western blot.

See also Figure S6.

FNIP1 co-depletion (Figure S7E). Mass spectrometry experiments showed that myoblasts derive few TCA cycle intermediates from glucose (Figure S7F), and the flux of glucose carbon atoms to the TCA cycle was unaffected by FEM1B depletion (Figure S7G). Co-depletion of glucose-utilizing enzymes also did not restore differentiation during reductive stress (Figure S7H). Thus, although FEM1B affects glucose metabolism, this likely involves a substrate distinct from FNIP1.

We noted that myoblasts derive most TCA cycle intermediates from glutamine (Figure S7F), which is converted into glutamate prior to its import into mitochondria. Metabolomics analyses found that FEM1B depletion decreased glutamate levels, whereas loss of FNIP1 increased its abundance (Figure 7E). Co-depletion of FEM1B and FNIP1 cancelled these phenotypes. In a similar manner, precursors or components of other mitochondrial shuttles were increased by FNIP1 loss, decreased upon depletion of

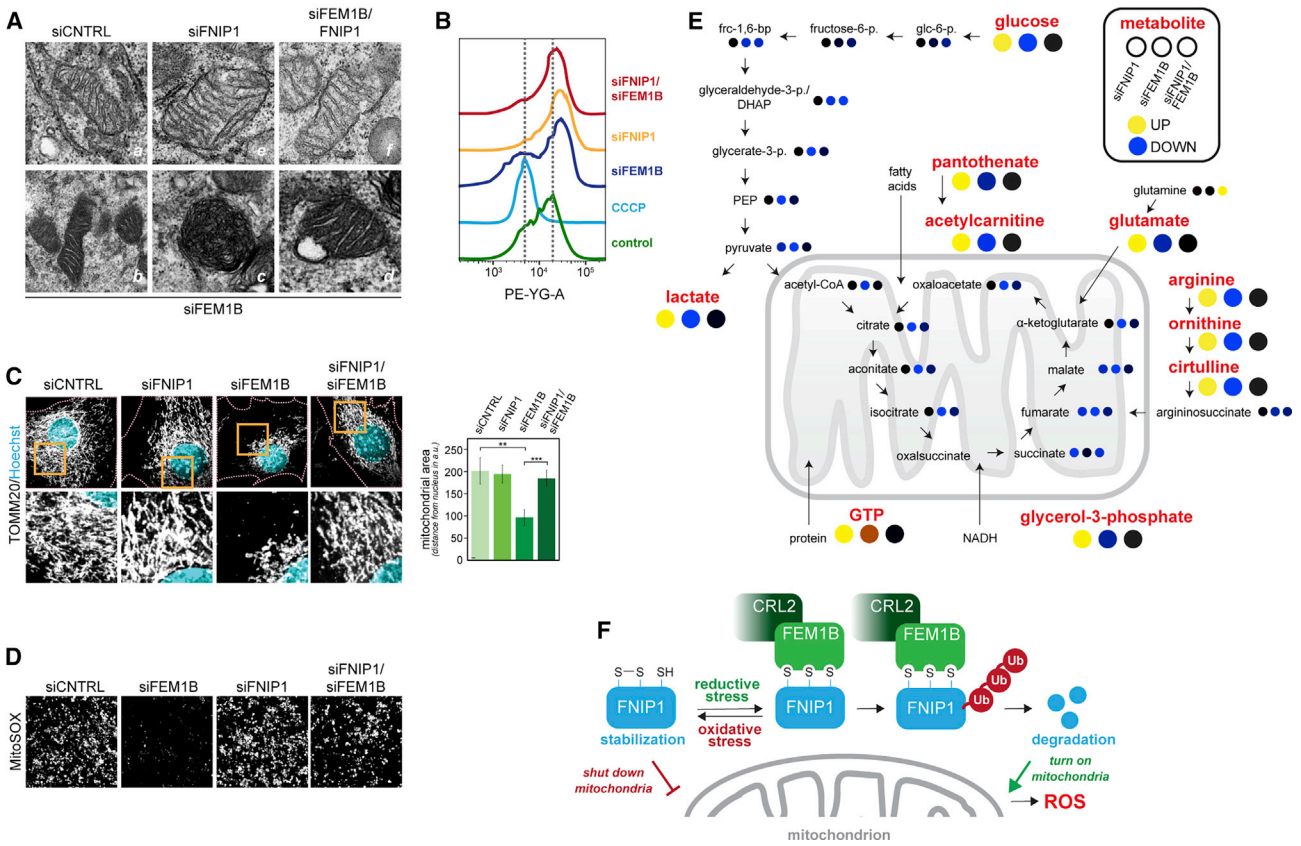

Figure 7. FNIP1 Is a Mitochondrial Gatekeeper

(A) C1C12 myoblasts were depleted of FEM1B, FNIP1, or both and processed for transmission electron microscopy.

(B) C2C12 myoblasts were depleted of FEM1B, FNIP1, or both; incubated with the mitochondrial membrane potential dye TMRM; and analyzed by flow cytometry (control: CCCP-treated cells).

(C) Mitochondrial morphology was examined in C2C12 myoblasts depleted of FNIP1, FEM1B, or both by immunofluorescence microscopy against TOMM20. The distance of mitochondria from the nucleus was quantified (n = 10–15 per condition).

(D) C2C12 myotubes were depleted of FEM1B, FNIP1, or both and stained for mitochondrial superoxide using MitoSox.

(E) C2C12 myoblasts were depleted of FEM1B and/or FNIP1, and the abundance of polar metabolites was determined by liquid chromatography and mass spectrometry. The first dot shows FNIP1-depleted cells, the second FEM1B-depleted cells, and the third cells co-depleted of FNIP1 and FEM1B (yellow, up-regulation compared with the control; blue, downregulation). Metabolites regulated by FNIP1 and FEM1B are depicted in red.

(F) Model of the reductive stress response. Reductive stress reverses the oxidation of invariant Cys residues in the FNIP1 degron, leading to recognition of FNIP1 by $CUL2^{FEM1B}$, polyubiquitylation, and proteasomal degradation. Loss of FNIP1 increases mitochondrial activity and triggers production of ROS to counteract reductive stress.

See also Figure S7.

FEM1B, and unaltered in myoblasts lacking FEM1B and FNIP1. This included citrulline and ornithine, which replenish fumarate from arginine; the fatty acid carrier acetylcarnitine and its precursor panthothenate; and the NADH shuttle glycerol-3-phosphate (Figure 7E). Degradation of FNIP1 through $CUL2^{FEM1B}$ therefore increases the availability of several metabolite shuttles, which could provide a means to jumpstart the TCA cycle and induce production of mitochondrion-derived ROS. We conclude that $CUL2^{FEM1B}$ and FNIP1 not only sense but also alleviate reductive stress, identifying these proteins as a core module of the reductive stress response.

DISCUSSION

Persistent lack of ROS, or reductive stress, impedes critical signaling pathways and increases mortality (Bjelakovic et al., 2007; McClung et al., 2004; Rajasekaran et al., 2007, 2011; Ristow et al., 2009). Although mitochondrial inactivity provides a physiological trigger for reductive stress, it is also elicited by inhibition of $CUL3^{KEAP1}$ and the ensuing accumulation of NRF2. KEAP1 inhibition is a frequent consequence of nutrient depletion, exposure to electrophilic toxins, or germline or somatic mutations (Bellezza et al., 2018; Bollong et al., 2018; Lignitto et al., 2019; Yamamoto et al., 2018). However, *KEAP1* deletion in mice causes lethality only after birth (Wakabayashi et al., 2003; Yamamoto et al., 2018), and *KEAP1* mutations are frequently observed in cancer cells (Armenia et al., 2018; Cancer Genome Atlas Research Network, 2012; Lignitto et al., 2019; Wiel et al., 2019). Thus, mechanisms must exist to detect and alleviate reductive stress.

Indeed, we identified $CUL2^{FEM1B}$ and its target FNIP1 as core components of the reductive stress response. $CUL2^{FEM1B}$ only

binds FNIP1 if the oxidation of Cys residues in FNIP1 is reverted during reductive stress. $CUL2^{FEM1B}$ then ubiquitylates FNIP1, which, in turn, activates mitochondria to counteract reductive stress (Figure 7F). We also found that $CUL2^{FEM1B}$ is required for nuclear import of NRF2, which, paradoxically, should support antioxidant gene expression. We speculate that the ability of $CUL2^{FEM1B}$ to license NRF2 nuclear import provides a safety mechanism during prolonged periods of FNIP1 degradation and mitochondrial activation. A similar dichotomy exists during oxidative stress, where NRF2 stabilization triggers antioxidant signaling and, likely with a delay, mitochondrial biogenesis (Rojo de la Vega et al., 2018). These findings highlight the importance of maintaining physiological ROS levels, which we now attribute to a redox rheostat that integrates oxidative and reductive stress responses.

Our findings suggest that FNIP1 degradation mainly acts as a mitochondrial gatekeeper. Stabilization of FNIP1 reduced mitochondrion-derived ROS and induced changes in mitochondrial morphology reminiscent of a lack of substrate for oxidative phosphorylation. Stable FNIP1 also depleted cells of metabolite shuttles, which reduced the levels of TCA cycle intermediates and dampened the reactions that generate substrate for the respiratory chain. FNIP1 stabilization could thus contribute to antioxidant defenses in cells with highly active mitochondria. FNIP1's role as a mitochondrial inhibitor might also be related to its recruitment to damaged mitochondria prior to autophagy because compromised organelles need to be shut down to ensure cell survival (Heo et al., 2018).

Importantly, reductive stress through its hallmark absence of ROS reduces the Cys degron in FNIP1 and triggers proteasomal degradation of this mitochondrial gatekeeper. Loss of FNIP1 boosted levels of metabolite shuttles, increased mitochondrial membrane potential, and restored mitochondrial activity in cells lacking FEM1B. These observations are congruent with phenotypes of *FNIP1* deletion in mice, which causes a switch from glycolytic to oxidative myofibers, characterized by abundant mitochondria (Reyes et al., 2015). We conclude that FNIP1 degradation increases mitochondrial output to produce ROS and counteract reductive stress. $CUL2^{FEM1B}$ and FNIP1 thus constitute a ubiquitin-dependent stress module that tunes mitochondrial output to the metabolic and redox needs of myoblasts (Figure 7F).

The reductive stress response bears striking similarity to pathways that respond to hypoxic and oxidative stress; these also rely on E3 ligases of the CRL family, which detect their substrates dependent on oxidation events. Although prolyl hydroxylation marks HIF1α for ubiquitylation by the hypoxic stress E3 $CUL2^{VHL}$ (Kaelin, 2007; Ohh et al., 2000), oxidation of Cys residues in KEAP1 prevents NRF2 ubiquitylation during oxidative stress (Zhang et al., 2004). It appears that cells evolved highly similar ubiquitin-dependent mechanisms to cope with different insults on redox homeostasis, which highlights the power of ubiquitylation to help cells adapt to rapidly changing environments.

Underscoring the importance of reductive stress signaling for tissue homeostasis, loss of FNIP1's partner FLCN results in predisposition to renal cancer (Baba et al., 2006; Nickerson et al., 2002). The same tumor type is caused by mutation of *KEAP1*, *CUL3*, *NFE2L2*, or *VHL* (Kaelin, 2007; Singh et al., 2006) or aberrant oxidative metabolism (Xu et al., 2019). Kidney cells might frequently fail to sustain the high ATP levels needed to filter toxic substrates out of blood (Bhargava and Schnellmann, 2017), a condition that resembles reductive stress. In line with the importance of ATP production, redox stress pathways shape energy metabolism; HIF1α increases glycolysis, NRF2 elicits mitochondrial biogenesis (Gonzalez et al., 2018; Rojo de la Vega et al., 2018), and FNIP1 tunes oxidative phosphorylation. Given the similar consequences of *KEAP1*, *FLCN*, and *VHL* mutation and their overlapping functions, we propose that it is regulation of metabolism that integrates the stress and developmental roles of these stress response pathways.

Although FNIP1 is its critical substrate during reductive stress, $CUL2^{FEM1B}$ also targets other proteins; CUL2 paired with FEM1A, FEM1B, or FEM1C ubiquitylates the histone mRNA-binding protein SLBP (Dankert et al., 2017), and FEM-1 binds Gli transcription factors in worms (Starostina et al., 2007). FEM1 proteins also act in the C-end rule pathway to eliminate proteins with carboxyl-terminal degrons or truncations (Koren et al., 2018). Because FEM1A does not bind FNIP1, it is likely that FEM1B detects these targets through a distinct site, potentially coordinating their degradation with redox regulation. We also found that $CUL2^{FEM1B}$ binds, but does not polyubiquitylate, the mTORC1 inhibitor GATOR1 (Bar-Peled et al., 2013; Dutchak et al., 2018). Opposite *FNIP1* deletion, which increases oxidative muscle fibers, muscle-specific loss of GATOR1 causes a switch to glycolytic fibers (Dutchak et al., 2018). We speculate that GATOR1 regulates FEM1B to prevent untimely FNIP1 degradation or coordinate reductive stress and mTORC1 signaling. Our discovery of the reductive stress response thus provides a starting point to dissect, and modulate for therapeutic benefit, the complex architecture of metazoan redox stress signaling, an important step toward elucidating how tissue homeostasis is accomplished in the natural environments of metazoan organisms.

STAR★METHODS

Detailed methods are provided in the online version of this paper and include the following:

- KEY RESOURCES TABLE
- RESOURCE AVAILABILITY
  - Lead Contact
  - Materials Availability
  - Data and Code Availability
  - Experimental Model and Subject Details
- METHOD DETAILS
  - Screening and myotube analysis
  - Transfection
  - Metabolomics
  - Small-scale Immunoprecipitations
  - Whole cell lysates
  - *In vitro* ubiquitylations
  - Flow Cytometry
  - *In vitro* binding
  - Fluorescence polarization
  - Protein purifications

- Seahorse analysis
- Immunofluorescence and confocal microscopy
- NAD/H NADP/H measurements
- H_2O_2 measurements
- ^{13}C labeling
- TUBE binding
- Glucose uptake assay
- Mitosox staining
- Antibodies
- Cloning
- shRNA production and viral production
- Quantitative real time PCR analysis
- Immunoprecipitation and mass spectrometry
- Genome editing
- NGS Library Prep and RNA-seq
- RNA-seq Alignment, Expression Analysis and Transcription Factor Enrichment
- Transmission electron microscopy

- QUANTIFICATION AND STATISTICAL ANALYSIS

SUPPLEMENTAL INFORMATION

Supplemental Information can be found online at https://doi.org/10.1016/j.cell.2020.08.034.

ACKNOWLEDGMENTS

We are grateful to Julia Schaletzky, David Savage, and members of the Rape and Nomura labs for discussions, advice, and reading the manuscript. We thank Roberto Zoncu for reagents and discussion. We also thank the staff, especially Reena Zalpuri, at the University of California, Berkeley, Electron Microscope Laboratory for assistance with electron microscopy sample preparation and data collection. We are grateful for the UC Berkeley Cancer Research Laboratory Flow Cytometry Facility. We thank Andrew Dillin for the use of an Agilent Seahorse Analyzer. This work used the University of California, Berkeley, Vincent J. Coates Genomics Sequencing Laboratory, supported by NIH S10 OD018174. A.G.M. was supported by a postdoctoral fellowship, PF-15-215-01 – DCC, from the American Cancer Society. F.R.-P. was supported by a Gilliam Fellowship of the Howard Hughes Medical Institute. We thank Dr. Mary West and Dr. Pingping He of the University of California, Berkeley, High-Throughput Screening Facility, funded by NIH award S10OD021828. We thank Anthony T. Iavarone of the QB3/Chemistry Mass Spectrometry Facility, supported by 1S10OD020062-01, for mass spectrometry assistance. M.R. is an Investigator of the Howard Hughes Medical Institute.

AUTHOR CONTRIBUTIONS

Conceptualization, A.G.M., F.R.-P., and M.R.; Methodology, A.G.M., F.R.-P., D.K.N., D.V.T., and M.R.; Investigation, A.G.M., F.R.-P., K.Y.S., Z.S., C.A.B., and M.C.; Writing – Original Draft, A.G.M. and M.R.; Writing – Reviewing & Editing, all authors; Funding Acquisition, A.G.M., F.R.-P., D.K.N., D.V.T., and M.R.; Supervision, D.K.N., D.V.T., and M.R.

DECLARATION OF INTEREST

M.R. is a co-founder and consultant to Nurix, a publicly traded company in the ubiquitin space. D.K.N. is a co-founder, shareholder, and adviser of Frontier Medicines.

Received: December 18, 2019
Revised: May 28, 2020
Accepted: August 18, 2020
Published: September 16, 2020

REFERENCES

Almada, A.E., and Wagers, A.J. (2016). Molecular circuitry of stem cell fate in skeletal muscle regeneration, ageing and disease. Nat. Rev. Mol. Cell Biol. *17*, 267–279.

Armenia, J., Wankowicz, S.A.M., Liu, D., Gao, J., Kundra, R., Reznik, E., Chatila, W.K., Chakravarty, D., Han, G.C., Coleman, I., et al.; PCF/SU2C International Prostate Cancer Dream Team (2018). The long tail of oncogenic drivers in prostate cancer. Nat. Genet. *50*, 645–651.

Avior, Y., Sagi, I., and Benvenisty, N. (2016). Pluripotent stem cells in disease modelling and drug discovery. Nat. Rev. Mol. Cell Biol. *17*, 170–182.

Baba, M., Hong, S.B., Sharma, N., Warren, M.B., Nickerson, M.L., Iwamatsu, A., Esposito, D., Gillette, W.K., Hopkins, R.F., 3rd, Hartley, J.L., et al. (2006). Folliculin encoded by the BHD gene interacts with a binding protein, FNIP1, and AMPK, and is involved in AMPK and mTOR signaling. Proc. Natl. Acad. Sci. USA *103*, 15552–15557.

Baba, M., Keller, J.R., Sun, H.W., Resch, W., Kuchen, S., Suh, H.C., Hasumi, H., Hasumi, Y., Kieffer-Kwon, K.R., Gonzalez, C.G., et al. (2012). The folliculin-FNIP1 pathway deleted in human Birt-Hogg-Dubé syndrome is required for murine B-cell development. Blood *120*, 1254–1261.

Bader, D., Masaki, T., and Fischman, D.A. (1982). Immunochemical analysis of myosin heavy chain during avian myogenesis in vivo and in vitro. J. Cell Biol. *95*, 763–770.

Balchin, D., Hayer-Hartl, M., and Hartl, F.U. (2016). In vivo aspects of protein folding and quality control. Science *353*, aac4354.

Banba, A., Tsuji, A., Kimura, H., Murai, M., and Miyoshi, H. (2019). Defining the mechanism of action of S1QELs, specific suppressors of superoxide production in the quinone-reaction site in mitochondrial complex I. J. Biol. Chem. *294*, 6550–6561.

Bar-Peled, L., Chantranupong, L., Cherniack, A.D., Chen, W.W., Ottina, K.A., Grabiner, B.C., Spear, E.D., Carter, S.L., Meyerson, M., and Sabatini, D.M. (2013). A Tumor suppressor complex with GAP activity for the Rag GTPases that signal amino acid sufficiency to mTORC1. Science *340*, 1100–1106.

Bellezza, I., Giambanco, I., Minelli, A., and Donato, R. (2018). Nrf2-Keap1 signaling in oxidative and reductive stress. Biochim. Biophys. Acta Mol. Cell Res. *1865*, 721–733.

Benjamin, D.I., Louie, S.M., Mulvihill, M.M., Kohnz, R.A., Li, D.S., Chan, L.G., Sorrentino, A., Bandyopadhyay, S., Cozzo, A., Ohiri, A., et al. (2014). Inositol phosphate recycling regulates glycolytic and lipid metabolism that drives cancer aggressiveness. ACS Chem. Biol. *9*, 1340–1350.

Bennett, E.J., Rush, J., Gygi, S.P., and Harper, J.W. (2010). Dynamics of cullin-RING ubiquitin ligase network revealed by systematic quantitative proteomics. Cell *143*, 951–965.

Bhargava, P., and Schnellmann, R.G. (2017). Mitochondrial energetics in the kidney. Nat. Rev. Nephrol. *13*, 629–646.

Bjelakovic, G., Nikolova, D., Gluud, L.L., Simonetti, R.G., and Gluud, C. (2007). Mortality in randomized trials of antioxidant supplements for primary and secondary prevention: systematic review and meta-analysis. JAMA *297*, 842–857.

Blondelle, J., Shapiro, P., Domenighetti, A.A., and Lange, S. (2017). Cullin E3 Ligase Activity Is Required for Myoblast Differentiation. J. Mol. Biol. *429*, 1045–1066.

Bollong, M.J., Lee, G., Coukos, J.S., Yun, H., Zambaldo, C., Chang, J.W., Chin, E.N., Ahmad, I., Chatterjee, A.K., Lairson, L.L., et al. (2018). A metabolite-derived protein modification integrates glycolysis with KEAP1-NRF2 signalling. Nature *562*, 600–604.

Brand, M.D., Goncalves, R.L., Orr, A.L., Vargas, L., Gerencser, A.A., Borch Jensen, M., Wang, Y.T., Melov, S., Turk, C.N., Matzen, J.T., et al. (2016). Suppressors of Superoxide-H_2O_2 Production at Site I_Q of Mitochondrial Complex I Protect against Stem Cell Hyperplasia and Ischemia-Reperfusion Injury. Cell Metab. *24*, 582–592.

Braun, T., and Gautel, M. (2011). Transcriptional mechanisms regulating skeletal muscle differentiation, growth and homeostasis. Nat. Rev. Mol. Cell Biol. *12*, 349–361.

Bray, N.L., Pimentel, H., Melsted, P., and Pachter, L. (2016). Near-optimal probabilistic RNA-seq quantification. Nat. Biotechnol. *34*, 525–527.

Buckley, S.M., Aranda-Orgilles, B., Strikoudis, A., Apostolou, E., Loizou, E., Moran-Crusio, K., Farnsworth, C.L., Koller, A.A., Dasgupta, R., Silva, J.C., et al. (2012). Regulation of pluripotency and cellular reprogramming by the ubiquitin-proteasome system. Cell Stem Cell *11*, 783–798.

Bullock, A.N., Debreczeni, J.E., Edwards, A.M., Sundström, M., and Knapp, S. (2006). Crystal structure of the SOCS2-elongin C-elongin B complex defines a prototypical SOCS box ubiquitin ligase. Proc. Natl. Acad. Sci. USA *103*, 7637–7642.

Cancer Genome Atlas Research Network (2012). Comprehensive genomic characterization of squamous cell lung cancers. Nature *489*, 519–525.

Cancer Genome Atlas Research Network (2013). Comprehensive molecular characterization of clear cell renal cell carcinoma. Nature *499*, 43–49.

Chen, J., Ou, Y., Yang, Y., Li, W., Xu, Y., Xie, Y., and Liu, Y. (2018). KLHL22 activates amino-acid-dependent mTORC1 signalling to promote tumorigenesis and ageing. Nature *557*, 585–589.

Dankert, J.F., Pagan, J.K., Starostina, N.G., Kipreos, E.T., and Pagano, M. (2017). FEM1 proteins are ancient regulators of SLBP degradation. Cell Cycle *16*, 556–564.

Denko, N.C. (2008). Hypoxia, HIF1 and glucose metabolism in the solid tumour. Nat. Rev. Cancer *8*, 705–713.

DeWitt, M.A., Corn, J.E., and Carroll, D. (2017). Genome editing via delivery of Cas9 ribonucleoprotein. Methods *121-122*, 9–15.

Dialynas, G., Shrestha, O.K., Ponce, J.M., Zwerger, M., Thiemann, D.A., Young, G.H., Moore, S.A., Yu, L., Lammerding, J., and Wallrath, L.L. (2015). Myopathic lamin mutations cause reductive stress and activate the nrf2/keap-1 pathway. PLoS Genet. *11*, e1005231.

Donato, V., Bonora, M., Simoneschi, D., Sartini, D., Kudo, Y., Saraf, A., Florens, L., Washburn, M.P., Stadtfeld, M., Pinton, P., and Pagano, M. (2017). The TDH-GCN5L1-Fbxo15-KBP axis limits mitochondrial biogenesis in mouse embryonic stem cells. Nat. Cell Biol. *19*, 341–351.

Dutchak, P.A., Estill-Terpack, S.J., Plec, A.A., Zhao, X., Yang, C., Chen, J., Ko, B., Deberardinis, R.J., Yu, Y., and Tu, B.P. (2018). Loss of a Negative Regulator of mTORC1 Induces Aerobic Glycolysis and Altered Fiber Composition in Skeletal Muscle. Cell Rep. *23*, 1907–1914.

Ezashi, T., Das, P., and Roberts, R.M. (2005). Low O2 tensions and the prevention of differentiation of hES cells. Proc. Natl. Acad. Sci. USA *102*, 4783–4788.

Furukawa, M., and Xiong, Y. (2005). BTB protein Keap1 targets antioxidant transcription factor Nrf2 for ubiquitination by the Cullin 3-Roc1 ligase. Mol. Cell. Biol. *25*, 162–171.

Gibson, D.G., Young, L., Chuang, R.Y., Venter, J.C., Hutchison, C.A., 3rd, and Smith, H.O. (2009). Enzymatic assembly of DNA molecules up to several hundred kilobases. Nat. Methods *6*, 343–345.

Gnarra, J.R., Ward, J.M., Porter, F.D., Wagner, J.R., Devor, D.E., Grinberg, A., Emmert-Buck, M.R., Westphal, H., Klausner, R.D., and Linehan, W.M. (1997). Defective placental vasculogenesis causes embryonic lethality in VHL-deficient mice. Proc. Natl. Acad. Sci. USA *94*, 9102–9107.

Gonzalez, F.J., Xie, C., and Jiang, C. (2018). The role of hypoxia-inducible factors in metabolic diseases. Nat. Rev. Endocrinol. *15*, 21–32.

Gores, G.J., Flarsheim, C.E., Dawson, T.L., Nieminen, A.L., Herman, B., and Lemasters, J.J. (1989). Swelling, reductive stress, and cell death during chemical hypoxia in hepatocytes. Am. J. Physiol. *257*, C347–C354.

Hackenbrock, C.R. (1966). Ultrastructural bases for metabolically linked mechanical activity in mitochondria. I. Reversible ultrastructural changes with change in metabolic steady state in isolated liver mitochondria. J. Cell Biol. *30*, 269–297.

Hasumi, H., Baba, M., Hong, S.B., Hasumi, Y., Huang, Y., Yao, M., Valera, V.A., Linehan, W.M., and Schmidt, L.S. (2008). Identification and characterization of a novel folliculin-interacting protein FNIP2. Gene *415*, 60–67.

Hasumi, H., Baba, M., Hasumi, Y., Huang, Y., Oh, H., Hughes, R.M., Klein, M.E., Takikita, S., Nagashima, K., Schmidt, L.S., and Linehan, W.M. (2012). Regulation of mitochondrial oxidative metabolism by tumor suppressor FLCN. J. Natl. Cancer Inst. *104*, 1750–1764.

Heo, J.M., Ordureau, A., Swarup, S., Paulo, J.A., Shen, K., Sabatini, D.M., and Harper, J.W. (2018). RAB7A phosphorylation by TBK1 promotes mitophagy via the PINK-PARKIN pathway. Sci. Adv. *4*, eaav0443.

Hermle, T., Schneider, R., Schapiro, D., Braun, D.A., van der Ven, A.T., Warejko, J.K., Daga, A., Widmeier, E., Nakayama, M., Jobst-Schwan, T., et al. (2018). *GAPVD1* and *ANKFY1* Mutations Implicate RAB5 Regulation in Nephrotic Syndrome. J. Am. Soc. Nephrol. *29*, 2123–2138.

Holmström, K.M., and Finkel, T. (2014). Cellular mechanisms and physiological consequences of redox-dependent signalling. Nat. Rev. Mol. Cell Biol. *15*, 411–421.

Huttlin, E.L., Ting, L., Bruckner, R.J., Gebreab, F., Gygi, M.P., Szpyt, J., Tam, S., Zarraga, G., Colby, G., Baltier, K., et al. (2015). The BioPlex Network: A Systematic Exploration of the Human Interactome. Cell *162*, 425–440.

Huttlin, E.L., Bruckner, R.J., Paulo, J.A., Cannon, J.R., Ting, L., Baltier, K., Colby, G., Gebreab, F., Gygi, M.P., Parzen, H., et al. (2017). Architecture of the human interactome defines protein communities and disease networks. Nature *545*, 505–509.

Itoh, K., Wakabayashi, N., Katoh, Y., Ishii, T., O'Connor, T., and Yamamoto, M. (2003). Keap1 regulates both cytoplasmic-nuclear shuttling and degradation of Nrf2 in response to electrophiles. Genes Cells *8*, 379–391.

Jiang, Y.F., Lin, S.S., Chen, J.M., Tsai, H.Z., Hsieh, T.S., and Fu, C.Y. (2017). Electron tomographic analysis reveals ultrastructural features of mitochondrial cristae architecture which reflect energetic state and aging. Sci. Rep. *7*, 45474.

Jin, S.M., Lazarou, M., Wang, C., Kane, L.A., Narendra, D.P., and Youle, R.J. (2010). Mitochondrial membrane potential regulates PINK1 import and proteolytic destabilization by PARL. J. Cell Biol. *191*, 933–942.

Jin, L., Pahuja, K.B., Wickliffe, K.E., Gorur, A., Baumgärtel, C., Schekman, R., and Rape, M. (2012). Ubiquitin-dependent regulation of COPII coat size and function. Nature *482*, 495–500.

Kaelin, W.G. (2007). Von Hippel-Lindau disease. Annu. Rev. Pathol. *2*, 145–173.

Keenan, A.B., Torre, D., Lachmann, A., Leong, A.K., Wojciechowicz, M.L., Utti, V., Jagodnik, K.M., Kropiwnicki, E., Wang, Z., and Ma'ayan, A. (2019). ChEA3: transcription factor enrichment analysis by orthogonal omics integration. Nucleic Acids Res. *47* (W1), W212–W224.

Koren, I., Timms, R.T., Kula, T., Xu, Q., Li, M.Z., and Elledge, S.J. (2018). The Eukaryotic Proteome Is Shaped by E3 Ubiquitin Ligases Targeting C-Terminal Degrons. Cell *173*, 1622–1635.e14.

Kovac, M., Navas, C., Horswell, S., Salm, M., Bardella, C., Rowan, A., Stares, M., Castro-Giner, F., Fisher, R., de Bruin, E.C., et al. (2015). Recurrent chromosomal gains and heterogeneous driver mutations characterise papillary renal cancer evolution. Nat. Commun. *6*, 6336.

Kwon, A.T., Arenillas, D.J., Worsley Hunt, R., and Wasserman, W.W. (2012). oPOSSUM-3: advanced analysis of regulatory motif over-representation across genes or ChIP-Seq datasets. G3 (Bethesda) *2*, 987–1002.

Lawrence, R.E., Fromm, S.A., Fu, Y., Yokom, A.L., Kim, D.J., Thelen, A.M., Young, L.N., Lim, C.Y., Samelson, A.J., Hurley, J.H., and Zoncu, R. (2019). Structural mechanism of a Rag GTPase activation checkpoint by the lysosomal folliculin complex. Science *366*, 971–977.

Leichert, L.I., Gehrke, F., Gudiseva, H.V., Blackwell, T., Ilbert, M., Walker, A.K., Strahler, J.R., Andrews, P.C., and Jakob, U. (2008). Quantifying changes in the thiol redox proteome upon oxidative stress in vivo. Proc. Natl. Acad. Sci. USA *105*, 8197–8202.

Lignitto, L., LeBoeuf, S.E., Homer, H., Jiang, S., Askenazi, M., Karakousi, T.R., Pass, H.I., Bhutkar, A.J., Tsirigos, A., Ueberheide, B., et al. (2019). Nrf2 Activation Promotes Lung Cancer Metastasis by Inhibiting the Degradation of Bach1. Cell *178*, 316–329.e18.

Lindahl, M., and Florencio, F.J. (2003). Thioredoxin-linked processes in cyanobacteria are as numerous as in chloroplasts, but targets are different. Proc. Natl. Acad. Sci. USA *100*, 16107–16112.

Louie, S.M., Grossman, E.A., Crawford, L.A., Ding, L., Camarda, R., Huffman, T.R., Miyamoto, D.K., Goga, A., Weerapana, E., and Nomura, D.K. (2016). GSTP1 Is a Driver of Triple-Negative Breast Cancer Cell Metabolism and Pathogenicity. Cell Chem. Biol. *23*, 567–578.

Mahrour, N., Redwine, W.B., Florens, L., Swanson, S.K., Martin-Brown, S., Bradford, W.D., Staehling-Hampton, K., Washburn, M.P., Conaway, R.C., and Conaway, J.W. (2008). Characterization of Cullin-box sequences that direct recruitment of Cul2-Rbx1 and Cul5-Rbx2 modules to Elongin BC-based ubiquitin ligases. J. Biol. Chem. *283*, 8005–8013.

McClung, J.P., Roneker, C.A., Mu, W., Lisk, D.J., Langlais, P., Liu, F., and Lei, X.G. (2004). Development of insulin resistance and obesity in mice overexpressing cellular glutathione peroxidase. Proc. Natl. Acad. Sci. USA *101*, 8852–8857.

Mena, E.L., Kjolby, R.A.S., Saxton, R.A., Werner, A., Lew, B.G., Boyle, J.M., Harland, R., and Rape, M. (2018). Dimerization quality control ensures neuronal development and survival. Science *362*, eaap8236.

Nickerson, M.L., Warren, M.B., Toro, J.R., Matrosova, V., Glenn, G., Turner, M.L., Duray, P., Merino, M., Choyke, P., Pavlovich, C.P., et al. (2002). Mutations in a novel gene lead to kidney tumors, lung wall defects, and benign tumors of the hair follicle in patients with the Birt-Hogg-Dubé syndrome. Cancer Cell *2*, 157–164.

Nusse, R., and Clevers, H. (2017). Wnt/β-Catenin Signaling, Disease, and Emerging Therapeutic Modalities. Cell *169*, 985–999.

Oh, E., Akopian, D., and Rape, M. (2018). Principles of Ubiquitin-Dependent Signaling. Annu. Rev. Cell Dev. Biol. *34*, 137–162.

Ohh, M., Park, C.W., Ivan, M., Hoffman, M.A., Kim, T.Y., Huang, L.E., Pavletich, N., Chau, V., and Kaelin, W.G. (2000). Ubiquitination of hypoxia-inducible factor requires direct binding to the beta-domain of the von Hippel-Lindau protein. Nat. Cell Biol. *2*, 423–427.

Orr, A.L., Vargas, L., Turk, C.N., Baaten, J.E., Matzen, J.T., Dardov, V.J., Attle, S.J., Li, J., Quackenbush, D.C., Goncalves, R.L., et al. (2015). Suppressors of superoxide production from mitochondrial complex III. Nat. Chem. Biol. *11*, 834–836.

Papizan, J.B., Vidal, A.H., Bezprozvannaya, S., Bassel-Duby, R., and Olson, E.N. (2018). Cullin-3-RING ubiquitin ligase activity is required for striated muscle function in mice. J. Biol. Chem. *293*, 8802–8811.

Pickles, S., Vigié, P., and Youle, R.J. (2018). Mitophagy and Quality Control Mechanisms in Mitochondrial Maintenance. Curr. Biol. *28*, R170–R185.

Pimentel, H., Bray, N.L., Puente, S., Melsted, P., and Pachter, L. (2017). Differential analysis of RNA-seq incorporating quantification uncertainty. Nat. Methods *14*, 687–690.

Rajasekaran, N.S., Connell, P., Christians, E.S., Yan, L.J., Taylor, R.P., Orosz, A., Zhang, X.Q., Stevenson, T.J., Peshock, R.M., Leopold, J.A., et al. (2007). Human alpha B-crystallin mutation causes oxido-reductive stress and protein aggregation cardiomyopathy in mice. Cell *130*, 427–439.

Rajasekaran, N.S., Varadharaj, S., Khanderao, G.D., Davidson, C.J., Kannan, S., Firpo, M.A., Zweier, J.L., and Benjamin, I.J. (2011). Sustained activation of nuclear erythroid 2-related factor 2/antioxidant response element signaling promotes reductive stress in the human mutant protein aggregation cardiomyopathy in mice. Antioxid. Redox Signal. *14*, 957–971.

Rajasekaran, N.S., Shelar, S.B., Jones, D.P., and Hoidal, J.R. (2020). Reductive stress impairs myogenic differentiation. Redox Biol. *34*, 101492.

Rape, M. (2018). Ubiquitylation at the crossroads of development and disease. Nat. Rev. Mol. Cell Biol. *19*, 59–70.

Reyes, N.L., Banks, G.B., Tsang, M., Margineantu, D., Gu, H., Djukovic, D., Chan, J., Torres, M., Liggitt, H.D., Hirenallur-S, D.K., et al. (2015). Fnip1 regulates skeletal muscle fiber type specification, fatigue resistance, and susceptibility to muscular dystrophy. Proc. Natl. Acad. Sci. USA *112*, 424–429.

Ristow, M., Zarse, K., Oberbach, A., Klöting, N., Birringer, M., Kiehntopf, M., Stumvoll, M., Kahn, C.R., and Blüher, M. (2009). Antioxidants prevent health-promoting effects of physical exercise in humans. Proc. Natl. Acad. Sci. USA *106*, 8665–8670.

Rodríguez-Colman, M.J., Schewe, M., Meerlo, M., Stigter, E., Gerrits, J., Pras-Raves, M., Sacchetti, A., Hornsveld, M., Oost, K.C., Snippert, H.J., et al. (2017). Interplay between metabolic identities in the intestinal crypt supports stem cell function. Nature *543*, 424–427.

Rojo de la Vega, M., Chapman, E., and Zhang, D.D. (2018). NRF2 and the Hallmarks of Cancer. Cancer Cell *34*, 21–43.

Schindelin, J., Arganda-Carreras, I., Frise, E., Kaynig, V., Longair, M., Pietzsch, T., Preibisch, S., Rueden, C., Saalfeld, S., Schmid, B., et al. (2012). Fiji: an open-source platform for biological-image analysis. Nat. Methods *9*, 676–682.

Sena, L.A., and Chandel, N.S. (2012). Physiological roles of mitochondrial reactive oxygen species. Mol. Cell *48*, 158–167.

Silverman, J.S., Skaar, J.R., and Pagano, M. (2012). SCF ubiquitin ligases in the maintenance of genome stability. Trends Biochem. Sci. *37*, 66–73.

Singh, A., Misra, V., Thimmulappa, R.K., Lee, H., Ames, S., Hoque, M.O., Herman, J.G., Baylin, S.B., Sidransky, D., Gabrielson, E., et al. (2006). Dysfunctional KEAP1-NRF2 interaction in non-small-cell lung cancer. PLoS Med. *3*, e420.

Skaar, J.R., Pagan, J.K., and Pagano, M. (2013). Mechanisms and function of substrate recruitment by F-box proteins. Nat. Rev. Mol. Cell Biol. *14*, 369–381.

Souza, R.W.A., Alves, C.R.R., Medeiros, A., Rolim, N., Silva, G.J.J., Moreira, J.B.N., Alves, M.N., Wohlwend, M., Gebriel, M., Hagen, L., et al. (2018). Differential regulation of cysteine oxidative post-translational modifications in high and low aerobic capacity. Sci. Rep. *8*, 17772.

Starostina, N.G., Lim, J.M., Schvarzstein, M., Wells, L., Spence, A.M., and Kipreos, E.T. (2007). A CUL-2 ubiquitin ligase containing three FEM proteins degrades TRA-1 to regulate C. elegans sex determination. Dev. Cell *13*, 127–139.

Stebbins, C.E., Kaelin, W.G., Jr., and Pavletich, N.P. (1999). Structure of the VHL-ElonginC-ElonginB complex: implications for VHL tumor suppressor function. Science *284*, 455–461.

Studer, L., Csete, M., Lee, S.H., Kabbani, N., Walikonis, J., Wold, B., and McKay, R. (2000). Enhanced proliferation, survival, and dopaminergic differentiation of CNS precursors in lowered oxygen. J. Neurosci. *20*, 7377–7383.

Suzuki, T., and Yamamoto, M. (2017). Stress-sensing mechanisms and the physiological roles of the Keap1-Nrf2 system during cellular stress. J. Biol. Chem. *292*, 16817–16824.

Tsai, J.J., Dudakov, J.A., Takahashi, K., Shieh, J.H., Velardi, E., Holland, A.M., Singer, N.V., West, M.L., Smith, O.M., Young, L.F., et al. (2013). Nrf2 regulates haematopoietic stem cell function. Nat. Cell Biol. *15*, 309–316.

Tsun, Z.Y., Bar-Peled, L., Chantranupong, L., Zoncu, R., Wang, T., Kim, C., Spooner, E., and Sabatini, D.M. (2013). The folliculin tumor suppressor is a GAP for the RagC/D GTPases that signal amino acid levels to mTORC1. Mol. Cell *52*, 495–505.

van der Reest, J., Lilla, S., Zheng, L., Zanivan, S., and Gottlieb, E. (2018). Proteome-wide analysis of cysteine oxidation reveals metabolic sensitivity to redox stress. Nat. Commun. *9*, 1581.

Vilchez, D., Simic, M.S., and Dillin, A. (2014). Proteostasis and aging of stem cells. Trends Cell Biol. *24*, 161–170.

Wakabayashi, N., Itoh, K., Wakabayashi, J., Motohashi, H., Noda, S., Takahashi, S., Imakado, S., Kotsuji, T., Otsuka, F., Roop, D.R., et al. (2003). Keap1-null mutation leads to postnatal lethality due to constitutive Nrf2 activation. Nat. Genet. *35*, 238–245.

Walker, D.W., and Benzer, S. (2004). Mitochondrial "swirls" induced by oxygen stress and in the Drosophila mutant hyperswirl. Proc. Natl. Acad. Sci. USA *101*, 10290–10295.

Wang, Y., Penfold, S., Tang, X., Hattori, N., Riley, P., Harper, J.W., Cross, J.C., and Tyers, M. (1999). Deletion of the Cul1 gene in mice causes arrest in early embryogenesis and accumulation of cyclin E. Curr. Biol. *9*, 1191–1194.

Werner, A., Iwasaki, S., McGourty, C.A., Medina-Ruiz, S., Teerikorpi, N., Fedrigo, I., Ingolia, N.T., and Rape, M. (2015). Cell-fate determination by ubiquitin-dependent regulation of translation. Nature *525*, 523–527.

Wickliffe, K.E., Lorenz, S., Wemmer, D.E., Kuriyan, J., and Rape, M. (2011). The mechanism of linkage-specific ubiquitin chain elongation by a single-subunit E2. Cell *144*, 769–781.

Wiel, C., Le Gal, K., Ibrahim, M.X., Jahangir, C.A., Kashif, M., Yao, H., Ziegler, D.V., Xu, X., Ghosh, T., Mondal, T., et al. (2019). BACH1 Stabilization by Antioxidants Stimulates Lung Cancer Metastasis. Cell *178*, 330–345.e22.

Winkelmann, J., Schormair, B., Lichtner, P., Ripke, S., Xiong, L., Jalilzadeh, S., Fulda, S., Pütz, B., Eckstein, G., Hauk, S., et al. (2007). Genome-wide association study of restless legs syndrome identifies common variants in three genomic regions. Nat. Genet. *39*, 1000–1006.

Wu, J., Jin, Z., Zheng, H., and Yan, L.J. (2016). Sources and implications of NADH/NAD(+) redox imbalance in diabetes and its complications. Diabetes Metab. Syndr. Obes. *9*, 145–153.

Xiao, W., and Loscalzo, J. (2020). Metabolic Responses to Reductive Stress. Antioxid. Redox Signal. *32*, 1330–1347.

Xu, J., Reznik, E., Lee, H.J., Gundem, G., Jonsson, P., Sarungbam, J., Bialik, A., Sanchez-Vega, F., Creighton, C.J., Hoekstra, J., et al. (2019). Abnormal oxidative metabolism in a quiet genomic background underlies clear cell papillary renal cell carcinoma. eLife *8*, e38986.

Yamamoto, M., Kensler, T.W., and Motohashi, H. (2018). The KEAP1-NRF2 System: a Thiol-Based Sensor-Effector Apparatus for Maintaining Redox Homeostasis. Physiol. Rev. *98*, 1169–1203.

Yau, R., and Rape, M. (2016). The increasing complexity of the ubiquitin code. Nat. Cell Biol. *18*, 579–586.

Zhang, D.D., Lo, S.C., Cross, J.V., Templeton, D.J., and Hannink, M. (2004). Keap1 is a redox-regulated substrate adaptor protein for a Cul3-dependent ubiquitin ligase complex. Mol. Cell. Biol. *24*, 10941–10953.

STAR★METHODS

KEY RESOURCES TABLE

REAGENT or RESOURCE	SOURCE	IDENTIFIER
Antibodies		
Mouse monoclonal anti-Flag clone M2	Sigma-Aldrich	Cat#F1804; RRID:AB_262044
Rabbit polyclonal anti-CUL2	Bethyl	Cat#A302-476A; RRID:AB_1944215
Rabbit monoclonal anti-FNIP1 [EPNCIR107]	Abcam	Cat#ab134969
Rabbit monoclonal anti-FNIP1 antibody [EPR20832]	Abcam	Cat#ab215725
Rabbit polyclonal anti-GFP	Abcam	Cat#ab6556; RRID:AB_305564
Rabbit polyclonal anti-FEM1B	Proteintech	Cat#19544-1-AP; RRID:AB_10644294
Mouse monoclonal anti-MYOSIN, SARCOMERE (MHC)	Developmental Studies Hybridoma Bank	Cat#MF 20; RRID:AB_2147781
Mouse monoclonal anti-MYOGENIN	Developmental Studies Hybridoma Bank	Cat#f5d; RRID:AB_2146602)
Mouse monoclonal anti-beta-ACTIN (clone C4)	MP Biomedicals	Cat#691001
Rabbit polyclonal Anti-TOMM20	Sigma-Aldrich	Cat#HPA011562; RRID:AB_1080326
Rabbit monoclonal anti-HA-Tag (C29F4)	Cell Signaling Technology	Cat#3724; RRID:AB_1549585
Rabbit monoclonal anti-Flag DYKDDDDK Tag	Cell Signaling Technology	Cat#2368; RRID:AB_2217020
Rabbit monoclonal anti-FLCN (D14G9)	Cell Signaling Technology	Cat#3697; RRID:AB_2231646
Rabbit monoclonal anti-KEAP1 (D6B12)	Cell Signaling Technology	Cat#8047; RRID:AB_10860776
Rabbit monoclonal anti-NRF2 (D1Z9C XP)	Cell Signaling Technology	Cat#12721; RRID:AB_2715528
Rabbit monoclonal anti-CITRATE SYNTHASE (D7V8B)	Cell Signaling Technology	Cat#14309; RRID:AB_2665545
Rabbit monoclonal anti-GAPDH (D16H11 XP)	Cell Signaling Technology	Cat#5174; RRID:AB_10622025
Rabbit monoclonal anti-Phospho-AMPKα (Thr172) (40H9)	Cell Signaling Technology	Cat#2535; RRID:AB_331250
Rabbit monoclonal anti-AMPKα (D5A2)	Cell Signaling Technology	Cat#5831; RRID:AB_1062218
Rabbit monoclonal anti-Phospho-p70 S6 KINASE (Thr389) (108D2)	Cell Signaling Technology	Cat#9234; RRID:AB_2269803
Rabbit monoclonal anti-p70 S6 KINASe (49D7)	Cell Signaling Technology	Cat#3661; RRID:AB_330337
Rabbit monoclonal anti-Phospho-ACETYL-COA CARBOXYLASE (Ser79)	Cell Signaling Technology	Cat#3661; RRID:AB_330337
Rabbit monoclonal anti-ACETYL-COA CARBOXYLASE (C83B10)	Cell Signaling Technology	Cat#3676; RRID:AB_2219397
Mouse monoclonal Anti-CUL3 clone 90	Mena et al., 2018	N/A
Bacterial and Virus Strains		
E.coli LOBSTR	Laboratory of Thomas Schwartz	N/A
E.coli: One Shot Stbl3 Chemically competent cells	Thermo Fisher Scientific	Cat#C737303
Chemicals, Peptides, and Recombinant Proteins		
TAMRA-labeled FNIP1 wild type peptide (5,6-TAMRA-RNKSSLLFKESEE TRTPNCNCKYCSHPVLG)	Koch Institute/MIT Biopolymers lab	N/A
TAMRA-labeled FNIP1 Cys-free peptide (5,6-TAMRA-RNKSSLLFKESEE TRTPNSNSKYSSHPVLG)	Koch Institute/MIT Biopolymers lab	N/A
TAMRA-labeled FNIP1 Lys-free peptide (5,6-TAMRA-RNRSSLLFRESEE TRTPNCNCRYCSHPVLG)	Koch Institute/MIT Biopolymers lab	N/A

(*Continued on next page*)

Continued

REAGENT or RESOURCE	SOURCE	IDENTIFIER
$^{MBP/HIS}$FEM1B	This paper	N/A
$^{MBP/HIS}$FEM1B/ELONGIN B/ ELONGIN C$^{17-112}$ complex	This paper	N/A
$^{HIS-TEV}$CUL2-RBX1	This paper	N/A
CUL2^{FEM1B} (CUL2-RBX1, FEM1B/ELONGIN B/ ELONGIN C$^{17-112}$ complex	This paper	N/A
E1/UBA1	Laboratory of Michael Rape	N/A
UBE2R1	Laboratory of Michael Rape	N/A
UBE2D3	Laboratory of Michael Rape	N/A
MBP-FBXL17	Laboratory of Michael Rape	N/A
GATOR1 complex (DEPDC5, ^{Flag} NPRL2, ^{Flag}NPRL3)	Laboratory of Roberto Zoncu	N/A
UBA3	Boston Biochem	Cat#E-313
UBE2M	Boston Biochem	Cat#E2-656
NEDD8	Boston Biochem	Cat#UL-812
UBIQUITIN	Boston Biochem	Cat#U-100H
$^{HIS-TEV-HALO}$4x UBIQUILIN UBA TUBE	MRC PPU, College of Life Sciences, University of Dundee, Scotland	Cat#DU23799
1,10-Phenanthroline	Sigma-Aldrich	Cat#P1,280-4
Hoechst 33342	AnaSpec	Cat#83218
cOmplete, EDTA-free protease inhibitor cocktail tablets from Roche	Sigma-Aldrich	Cat#11873580001
Phenylmethanesulfonyl fluoride	Sigma-Aldrich	Cat#P7626
Polyethylenimine (PEI), Linear, MW 25000, Transfection Grade	Polysciences	Cat#23966-1
iodoacetamide	Thermo Fisher Scientific	Cat#A39271
N-Ethylmaleimide	Sigma-Aldrich	Cat#E3876
TEV protease	UC Berkeley QB3 MacroLab	N/A
^{13}C glucose	Sigma-Aldrich	Cat#389374-1G
isotopic AMP	Sigma-Aldrich	Cat#900382
isotopic Fructose-1,6-bisphosphate	Cambridge Isotope Laboratories	Cat#CLM-6678-0
MitoSox	Invitrogen	Cat#M36008
3xFlag peptide	Millipore	Cat#F4799
S1QEL1.1	Sigma-Aldrich	Cat#SML1948
S3QEL 2	Sigma-Aldrich	Cat#SML1554
Z-Leu-Leu-Leu-al (MG132)	Thermo Fisher Scientific	Cat#I13005M
IA-Alkyne	Tocris	Cat#7015
Bardoxolone methyl	Sigma-Aldrich	Cat# SMB00376
TCEP (Tris(2-carboxyethyl)phosphine hydrochloride))	Sigma-Aldrich	Cat#C4706
Carfilzomib	Selleck Chemical	Cat#PR-171
Oligomycin	Thermo Fisher Scientific	Cat#ICN15178601
TBHQ (tert-Butylhydroquinone)	Acros organic	Cat#150820050
MLN4924	Cayman Chemicals	Cat#15217
CCCP (CARBONYL CYANIDE 3-CHLOROPHENYLHYDRAZONE)	Sigma-Aldrich	Cat#C2759
Rotenone	Sigma-Aldrich	Cat#R8875
Myxothiazol	Sigma-Aldrich	Cat#T5580

(*Continued on next page*)

Continued

REAGENT or RESOURCE	SOURCE	IDENTIFIER
Dimethyl 2-oxoglutarate (aKG)	Sigma-Aldrich	Cat#349631
Antimycin A	Sigma-Aldrich	Cat#A8674
Critical Commercial Assays		
MitoProbe TMRM Assay Kit for Flow Cytometry	Thermo Fisher Scientific	Cat#M20036
NAD/NADH-Glo	Promega	Cat#G9072
NADP/NADPH-Glo	Promega	Cat#G9082
ROS-Glo H2O2 Assay	Promega	Cat#G8820
Glucose Uptake-Glo Assay	Promega	Cat#J1341
Seahorse XF Cell Mito Stress Test	Agilent	Cat#103015-100
Seahorse XF Glycolytic Rate Assay	Agilent	Cat#103710-100
TnT quick coupled *in vitro* transcription/translation system	Promega	Cat#L2080
Ioninc Detergent Compatibility Reagent	Thermo Fisher Scientific	Cat#22663
Pierce 660nm Protein Assay Reagent	Thermo Fisher Scientific	Cat#22660
Deposited Data		
RNaseq of C2C12 cells depleted of KEAP1 and/or FEM1B		GSE155374
Experimental Models: Cell Lines		
HEK293T	ATCC	Cat#CRL-3216; RRID: CVCL_0063
C2C12	ATCC	Cat#CRL-1772 RRID:CVCL_0188
Human: FLAG-FEM1B HEK293T cells	This paper	N/A
Human: FEM1BΔ #1 (LA3) HEK293T cells	This paper	N/A
Human: FEM1BΔ #2 (SG2) HEK293T cells	This paper	N/A
Human: FEM1BΔ #3 (SA4) HEK293T cells	This paper	N/A
SF9	ATCC	Cat# CRL-1711; RRID:CVCL_0549
Oligonucleotides		
Primer for FEM1B sgRNA (KO): ggatcctaatacgactcactatagATT AACGAGTCCGCGCGCGTgt tttagagctagaa	This paper	N/A
Primer for FEM1B sgRNA (KO): ggatcctaatacgactcactatagAA GACGAGCTTTCGCAGACA gttttagagctagaa	This paper	N/A
Fwd primer for FEM1B sgRNA (tagging): caccGGCGGCGGCCATGGAGGGCC	This paper	N/A
Rev primer for FEM1B sgRNA tagging: aaacGGCCCTCCATGGCCGCCGCC	This paper	N/A
Donor oligo DNA for FLAG tag insertion at the N terminus of FEM1B: TCCGGGGGCGCAC GGCAGCTGCAGCGGTGGC GACCAAACGGGTGTTGGA GTTGGCGGCGGCCATGG ACTACAAAGACCATGACGG TGATTATAAAGATCATGACA TCGATTACAAGGATGACGAT GACAAGGAGGGCCTGGCT GGCTATGTATACAAGGCGG CCAGCGAGGGCAAGGTGCT GACTCTGGCCGCCTTGCTT	This paper	N/A
shFEM1B$^{\#1}$	Sigma-Aldrich	Cat#SHCLNG TRCN0000303677125

(*Continued on next page*)

Continued

REAGENT or RESOURCE	SOURCE	IDENTIFIER
shFEM1B$^{\#2}$	Sigma-Aldrich	Cat#SHCLNG TRCN0000299671125
shFEM1B$^{\#3}$	Sigma-Aldrich	Cat#SHCLNG TRCN0000303647125
shFEM1B$^{\#4}$	Sigma-Aldrich	Cat#SHCLNG TRCN0000303746125
shTXNRD1	Sigma-Aldrich	Cat#SHCLNG TRCN0000046535
shGSR	Sigma-Aldrich	Cat#SHCLNG TRCN0000046425
See Table S2 for all siRNA targeting sequences		
See Table S3 for all qPCR primer sequences		
Recombinant DNA		
pCS2+ 3xFlag-FEM1B (wild-type, L597A, C186S)	This paper	N/A
pCS2+ HA-FLCN	This paper	N/A
pCS2+ HA-FNIP1 (wild-type, 1-893, 1-704, 1-560, 561-1137, 561-893, 562-591, 562-578Δ, 572-581Δ, 582-591Δ, 592-632Δ, S572A, E574R, E574R, T575A, R576A, T577A, P578A, N579A, C580S, N581A, C582S, K583A, Y584F, C585S, S586A, H587A, and C580S/C582S/C585S)	This paper	N/A
pCS2+ Flag-FNIP1 (wild-type and C580S/C582S/C585S)	This paper	N/A
pCS2+ HA-DEPDC5	This paper	N/A
pCS2+ HA-NPRL2	This paper	N/A
pCS2+ HA-NPRL3	This paper	N/A
pCS2+ HA-dnCUL2 (1-427)	This paper	N/A
pCS2+ GFP-2xEsp3I-IRES-mCherry	This paper	N/A
pCS2+ GFP-Fnip1 degron (562-591)-IRES-mCherry (wild-type, C580S, C582S, C585S, C580S/C582S, and C580S/C582S/C585S)	This paper	N/A
pCS2+ TRX-HIS6-Flag C35S	This paper	N/A
pMAL MBP-TEV2x-HIS6-FEM1B	This paper	N/A
pRSFDuet-1 Elongin B, ElonginC$^{17-112}$	This paper	N/A
pFastBac Dual HIS6-TEV-CUL2, RBX1	This paper	N/A
pET28a-6HIS-TEV-HALO-4x ubiquilin UBA TUBE	MRC PPU, College of Life Sciences, University of Dundee, Scotland	DU23799
pX330-sgRNA-FEM1B	This paper	N/A
pLenti-PGK-Hygro-Flag-CUL2	This paper	N/A
Software and Algorithms		
GraphPad Prism	GraphPad Software, Inc	RRID:SCR_002798
Metamorph Advanced	Molecular Devices	RRID:SCR_002368
FlowJo	Flowjo	RRID:SCR_008520
Columbus Image Data Storage and Analysis System	PerkinElmer	Cat#Columbus
Harmony High-Content Imaging and Analysis Software	PerkinElmer	Cat#HH17000010
Fiji	Schindelin et al., 2012	RRID:SCR_002285
Kallisto	Bray et al., 2016	RRID:SCR_016582
Sleuth	Pimentel et al., 2017	RRID:SCR_016883
Other		
Lipofectamine RNAiMAX	Thermo Fisher Scientific	Cat#13778150
Lipofectamine 2000	Thermo Fisher Scientific	Cat#11668027
ANTI-FLAG® M2 Affinity Agarose Gel slurry	Sigma-Aldrich	Cat#A2220

(*Continued on next page*)

Continued

REAGENT or RESOURCE	SOURCE	IDENTIFIER
Ni-NTA	QIAGEN	Cat#30210
HiLoad 16/600 Superdex 200pg	GE Healthcare	Cat#28-9893-35
Mono Q 10/100 GL	GE Healthcare	Cat#17-5167-01
HALO-link resin	Promega	Cat#G1914
3xFlag peptide	Millipore	Cat#F4799
Protein G-Agarose beads	Roche	Cat#11719416001
Amylose Resin	New England Biolabs	Cat#E8021L

RESOURCE AVAILABILITY

Lead Contact

Further information and requests for reagents and resources should be directed to the Lead Contact Michael Rape (mrape@berkeley.edu).

Materials Availability

All plasmids and cell lines generated in this work can be requested from the lead contact's lab. All antibodies, chemicals, and most cell lines used in this study are commercially available.

Data and Code Availability

Gene expression data by RNaseq from cells lacking KEAP1, FEM1B, or both were uploaded to GEO (GSE155374).

Experimental Model and Subject Details

C2C12 myoblasts (ATCC, CRL-1772, female) and HEK293Ts (ATCC, CRL-3216, female) were grown in DMEM with 10% fetal bovine serum at 37°C and 5% CO_2. For C2C12 differentiation, cells were grown to 70%–90% confluence and had their media changed 2-3x in differentiation medium, DMEM with 2% donor equine serum. For amino acid starvation, cells were washed 1x in PBS and put in amino acid free RPMI (US biologicals, R9010-01) and 10% dialyzed FBS. 1x Amino acids were added to the cultures at indicated time points. For glucose and glutamine starvations, cells were rinsed in phosphate buffered saline and incubated with DMEM -Glucose (Thermo Fisher Scientific, 11966025) or DMEM -Glutamine (Thermo Fisher Scientific, 11960044) with 10% dialyzed fetal bovine serum. SF9 (ATCC, CRL-1711, female) insect cell cultures were grown in in ESF921 (Expression Systems) supplemented with 1% fetal bovine serum and 1% Antibiotic-Antimycotic (Thermo Fisher Scientific, 15240062) at 28°C with shaking at 125rpm. All cell stocks and SF9 cultures were obtained from the UCB Cell Culture Facility which is supported by The University of California Berkeley.

METHOD DETAILS

Screening and myotube analysis

For the CUL2 and CUL3 adaptor screen, early passage C2C12 mouse myoblasts were seeded into 96 well plates at 400 to 500 cells/well using a Thermo Scientific Mulitdrop Combi system. The next day, cells were transfected with ~20nM final concentration of siRNAs using an Agilent Velocity 11 Bravo Automated Liquid Handling Platform. The next day, cells were differentiated by changing the media 3x with differentiation media using the Bravo. Media was changed every day and on the fourth day, cells were fixed in 4% formaldehyde in PBS for 20min. Fixed cells were washed in PBS, permeabilized with 0.1% triton, and stained for immunofluorescence with antibodies in phosphate buffered saline with 10% fetal bovine serum. All incubations for immunofluorescence were done with very slow mixing in a circular motion on a plate shaker for 3 hours for primary antibody and 1 hour for secondary antibody and Hoechst (AnaSpec, 83218). Plates were imaged on a Molecular Devices ImageXpress Micro Widefield High-Content Analysis System with a 10x objective capturing 25 images per well. Images were analyzed by a MetaXpress custom module from Molecular Devices to quantify the myotube area and nuclei count.

Individual siRNA myotube analysis was performed as described above, but with 12 well plates seeded with early passage C2C12 cells at 40,000-50,000 cells per well. The day after seeding, cells were transfected with 20-80nM final concentration of siRNAs depending on the number of co-depletions. For S1QEL1.1 and S3QEL 2 myotube analysis, 12-14 hours after siRNA transfection, the media was replaced with growth media containing DMSO or 1.75 μM S1QEL1.1 and 42.5 μM S3QEL 2 (Sigma-Aldrich, SML1948 and SML1554). These drug concentrations were maintained for all subsequent media changes throughout differentiation. Cells were fixed at day 3 or 4 of differentiation and prepared for immunofluorescence as above. 49 or 100 images per condition were acquired on Perkin Elmer Opera Phenix automated microscope using a 20x objective. Images were analyzed by an analysis sequence designed in the Perkin Elmer Harmony and Columbus software to quantify a fusion index (nuclei within MyHC stained cells containing 2 or more

nuclei divided by the total nuclei). The analysis of the cullin depletion phenotypes and the initial validation of screen hits were performed on the ImageXpress Micro.

Transfection

For transient plasmid transfection, 293Ts and C2C12s were transfected using polyethylenimine (PEI, Polysciences 23966-1) with cDNAs expressed from pCS2+ vectors. For the C2C12 FEM1B mass spectrometry immunoprecipitations, 20ug of DNA with 60μl of PEI (1mg/ml) in 500μl Optimem per 15 cm with a total of 20 plates. For 293T experiments, the following μg amounts were used for 10cm plate transfections ^{HA}FNIP1 constructs 2 μg, ^{HA}FLCN 0.5-1 μg, ^{Flag}FEM1B constructs 0.5-1 μg, ^{HA}DEPDC5 0.5 μg, ^{HA}NPRL2 0.5 μg, ^{HA}NPRL3 0.5 μg, dnCUL2$^{1-427}$-HA 5 μg, ^{GFP}degron-IRES-mCherry reporters 0.1 μg, and TRX^{C35S}-HIS6/Flag 0.6 μg. PEI ratios 1:3 to 1:6 μg DNA to μl of PEI were used in 300μl of Optimum and cells were harvested 36h after transfection. For the FNIP1 mass spectrometry immunoprecipitation, 10x15cm plates of 293Ts were transfected with 1.5 μg ^{Flag}FNIP1, 0.75 μg ^{HA}FLCN and empty vector to 4 μg total with 1:6 ratio of PEI in 400μl Optimem per plate. For the purification of ^{Flag}FNIP1/^{HA}FLCN for *in vitro* ubiquitylation reactions, 4 μg of ^{Flag}FNIP1 and 2 μg of ^{HA}FLCN transfected as for the mass spectrometry transfection into 10x15cm plates of 293T. For flow cytometry, 0.1 μg of ^{GFP}degron-IRES-mCherry reporters, 1 μg of FEM1B constructs, and empty vector to 2 μg total were added to 300μl of Optimum and 12μl PEI (1:6 ratio) and 60μl were added to 6 well plates of 293Ts and harvested for flow cytometry after 24h. siRNA transfections were performed with Lipofectamine RNAiMAX (Thermo Fisher Scientific, 13778150) according to the manufacturer's recommendation. All siRNAs were ordered from Dharmacon/Horizon. Table S2 contains all siRNA sequences and catalog numbers.

Metabolomics

Metabolomics for polar metabolites were performed as described (Louie et al., 2016) on 5 replicate 10cm of plates of C2C12 myoblast transfected with indicated siRNAs for 36 hours. Briefly, frozen cell pellets were extracted in 40:40:20 acetonitrile:methanol:-water with inclusion of internal standard. Samples were vortexed and sonicated under pellets were in solution and then subjected to centrifugation at 13,000 x g for 15 min. Supernatant was isolated for single-reaction monitoring (SRM)-based targeted LC-MS/MS. Metabolites were separated using normal-phase chromatography using a Luna 5 mm NH2 column (50 × 4.6 mm, Phenomenex). Mobile phases were as followed, buffer A: acetonitrile, buffer B: 95:5 water:acetonitrile with 0.1% formic acid or 0.2 ammonium hydroxide with 50 mM ammonium acetate for positive and negative ionization mode, respectively. Chromatography conditions are as described previously (Benjamin et al., 2014). MS analysis was performed using an Agilent 6430 QQQ LC-MS/MS where metabolites were detected by single-reaction monitoring (SRM) and quantified by integrating the area under the curve for each metabolite and subsequent normalization to internal standard levels. Metabolites were then normalized to control samples.

Small-scale Immunoprecipitations

Cells were harvested by removing growth media and scraping cells in 8-10ml of cold PBS. Cells were centrifuged for 5min at 300 g and pellets resuspended in lysis buffer (40mM HEPES 7.5, 150mM NaCl, 0.2% NP40, with Roche cOmplete Protease Inhibitor Cocktail (Sigma-Aldrich, 11873580001)). For Figure S2D, the lysis buffer contained 2mM 1,10-Phenanthroline (Sigma-Aldrich, P1,280-4). For Figure 6G, lysis buffer was the same as for FNIP1 mass spectrometry immunoprecipitation (40mM HEPES 7.5, 150mM NaCl, 0.2% NP40, with Roche cOmplete Protease Inhibitor Cocktail, 10mM β-glycerol phosphate, 10mM sodium pyrophosphate, 2.5mM $MgCl_2$). Lysates were gently rocked for 30-60min at 4°C and cleared by centrifugation for 30min at 21000 g, 4°C. Supernatants were normalized to volume and protein concentration (if cells were treated with aromatic compounds, lysates were normalized using pierce 660nm). 5% of the sample was removed as an input and of the sample was added to 20μl of washed ANTI-FLAG® M2 Affinity Agarose Gel slurry (Sigma-Aldrich, A2220) and rotated for 1-2 hours at 4°C. Beads were washed three times and eluted with 2x urea sample buffer. For indicated TRX^{C35S} immunoprecipitations, cells were treated for 16 hours with Antimycin A (250nM, Sigma-Aldrich), Dimethyl 2-oxoglutarate (αKG) (10μM, Sigma-Aldrich), and Bardoxolone methyl (400nM, Sigma-Aldrich). For the ^{Flag}FEM1B immunoprecipitations in Figures 6G and 6H cells were treated with CCCP (10 μM, 1h, Sigma-Aldrich; Figure 6G only), Oligomycin (10 μM, 12h, Sigma-Aldrich), Antimycin A (10 μM, 12h, Sigma-Aldrich), and TBHQ (100 μM, 12h, Acros organic).

Whole cell lysates

For western blot time courses, C2C12 myoblasts were seeded in 12 well plates at 40-50k cells per well. Cells were transfected 24h later with siRNAs at 20nM-40nM for each siRNA. 24h after transfection, cells were differentiated, harvested at indicated time points by washing in PBS, and lysed in 2x urea sample buffer, heated to 65°C for 10min, sonicated, and normalized to protein concentration and volume with Pierce 660nm Protein Assay Reagent with Ioninc Detergent Compatibility Reagent (Thermo Fisher Scientific, 22660 and 22663). For Western analysis of phosphorylated proteins and of 293T cells, cells in 6-well plates were washed in cold PBS and harvested in lysis buffer (1% Triton X-100, 10mM β-glycerol phosphate, 10mM sodium pyrophosphate, 4mM EDTA, 40mM HEPES, pH7.4 with Roche cOmplete Protease Inhibitor Cocktail) with rocking for 10min at 4°C. Cell lysates were collected in 1.7ml tubes and rocked for additional 20min at 4°C. Cells lysates were cleared by centrifugation at 21,000 gs for 20min at 4°C. Supernatants were collected, normalized with Pierce 660nm, and added to an equal volume of 2x urea sample buffer. For the MG132 treatment in Figure 3G, 10 μM MG132 (Thermo Fisher Scientific, I13005M) was added for 6 hours prior to harvesting. Samples were heated to 65°C for 10min and analyzed by immunoblot with indicated antibodies.

In vitro ubiquitylations

For all ubiquitylations, CUL2-RBX1 and CRL2^{FEM1B} complexes were modified with NEDD8 prior to the ubiquitylation assay in UBA buffer (50mM Tris-HCl pH 7.5, 50mM NaCl, 10mM $MgCl_2$), 20mM ATP, 6.3μM Nedd8, 1mM DTT, 5μM CUL2 complexes, 700nM UBA3, 400nM UBE2M in a 20μl reaction volume for 15min at 30°C. Ubiquitylation assays were carried out in 10μl reactions with 1μM CUL2 ligase, 100μM ubiquitin, 1x UBA buffer (50mM Tris-HCl pH 7.5, 50mM NaCl, 10mM $MgCl_2$) 20mM ATP, 1mM DTT, 1μM E2s, and 1μM UBA1. For full length ^{Flag}FNIP/^{HA}FLCN, 1-2μl of buffer exchanged αFLAG elutions were used and reactions carried out at 30°C for 1h. For peptides, 500nM final concentration of 5,6-TAMRA labeled peptides were incubated at 30°C for indicated times. To alkylate with iodoacetamide (Thermo Fisher Scientific, A39271) and N-Ethylmaleimide (Sigma-Aldrich, E3876), 200μM peptide was incubated with or without 600μM alkylating agent for 1hour. Peptides were diluted into binding buffer with 0.1mM DTT to quench the alkylating agents before addition into ubiquitylation reactions.

Flow Cytometry

293T cells were seeded at 300k cell/well in 6 well plates. The next day, cells were transfected with indicated constructs. Cells were treated with the following reagents at indicated times before harvesting: IA-Alkyne (20μM, 8h, Tocris), Antimycin A (250nM, 16h, Sigma-Aldrich), Carfilzomib (2μM, 8h, Selleck Chemical), Dimethyl 2-oxoglutarate (αKG) (10μM, 8h, Sigma-Aldrich), Bardoxolone methyl (3μM, 8h, Sigma-Aldrich), Rotenone (250 or 500nM, 16h, Sigma-Aldrich), and Myxothiazol (100nM, 16h, Sigma-Aldrich). 24h post transfection, cells were trypsinized and centrifuged at 300 g for 5min. Cells were resuspended in full media with 10% FBS and analyzed on either BD Bioscience LSR Fortessa or LSR Fortessa X20 and FlowJo. For TMRM staining, 150,000 C2C12 myoblasts were seeded in 10 cm plates. The next day, cells were transfected with siRNAs and after 24h medium was exchanged. Cells were trypsinized 36-40h post transfection and counted. 1,000,000 cells were aliquoted in 1ml of pre-warmed PBS and labeled. A control sample was pretreated with 50 μM CCCP for 5min and all samples were labeled with 20nM TMRM from the MitoProbe TMRM Assay Kit for Flow Cytometry (Thermo Fisher Scientific, M20036) for 30min at 37°C in 5% CO_2. Cells were washed in warm PBS and analyzed on BD Bioscience LSR Fortessa and FlowJo.

In vitro binding

pCS2+-^{HA}FNIP1$^{561-893}$ was synthesized using the rabbit reticulocyte lysate TnT quick coupled *in vitro* transcription/translation system (Promega, L2080) as directed. Translated ^{HA}FNIP1$^{561-893}$ reactions were diluted in binding buffer (40mM HEPES 7.5, 150mM NaCl, 0.2% NP40, with or without 2mM TCEP and with or 2mM iodoacetamide) and added to amylose beads (New England Biolabs, E8021L) with bound ^{MBP}FEM1B or MBP. Samples were rocked at room temperature for 1h and washed in binding buffer with or without TCEP. Samples were eluted in urea sample buffer and analyzed by immunoblot with indicated antibodies.

Fluorescence polarization

TAMRA-labeled FNIP1 peptides (5,6-TAMRA-RNKSSLLFKESEETRTPNCNCKYCSHPVLG) and mutants were purchased from the Koch Institute/MIT Biopolymers lab. Binding titrations were performed with 50nM ^{TAMRA}FNIP1 peptides and increasing protein concentrations in binding buffer (40mM HEPES 7.5, 150mM NaCl, 0.2% NP40, with or without 0.1mM TCEP) in triplicate. For iodoacetamide and N-Ethylmaleimide peptide labeling, 200μM peptide was labeled with 600μM alkylating agent for 1h. Peptides were diluted into binding buffer with 0.1mM DTT to quench the alkylating agents before mixing with protein. Fluorescence polarization measurements were performed on BioTek Synergy H4 plate reader after 1h of incubation at room temp. Data was analyzed with GraphPad using the specific binding fit with Hill slope equation.

Protein purifications

Mouse $^{MBP/HIS}$FEM1B (pMAL, New England Biolabs) and the $^{MBP/HIS}$FEM1B/Elongin B/Elongin C$^{17-112}$ complex (pRSFduet-1, Novagen) were purified from *E.coli* LOBSTR cells grown to OD_{600} 0.5 and induced with 333μM IPTG overnight at 16°C. Cells were lysed in buffer A and added to 1/2 the lysate volume of buffer B (50mM HEPES 7.5, 300mM NaCl 1.5mM PMSF, 15mM β-mercaptoethanol, and 30mM Imidazole). Cells were sonicated and spun at 30,000xg for 1h. Supernatant was added to Ni-NTA slurry and bound for 1h at 4°C. Beads were washed in wash buffer (50mM HEPES 7.5, 150mM NaCl, 5mM β-mercaptoethanol, 20mM imidazole, and 1mM PMSF) three times for 15min with rocking. Beads were eluted with 50mM HEPES 7.5, 150mM NaCl, 5mM β-mercaptoethanol, 250mM imidazole. Elutions were dialyzed overnight and ran on a HiLoad 16/600 Superdex 200pg, concentrated, aliquoted, and flash frozen. $^{MBP/HIS}$FEM1B was purified without reducing agent for FP assays as above, but run on the size exclusion column in the absence of reducing agents. For CUL2-RBX1 purification, $^{HIS/TEV}$CUL2 and untagged RBX1 were expressed off the pFastBac Dual vector (Thermo Fisher Scientific, 10712024). Baculovirus packaging and amplification were performed as described (Bac-to-Bac Baculovirus Expression System, Thermo Fisher Scientific). For the purification, 3L of SF9 insect cells were infected and 72 hours later harvested by centrifugation and flash frozen in liquid nitrogen. Cells were lysed in 50mM HEPES 7.5, 150mM NaCl 1mM PMSF, 5mM β-mercaptoethanol, 10mM Imidazole, and 0.5% NP40 with gentle rocking at 4°C for 1h. Lysates were centrifuged at 30,000xg for 1h ^{HIS}CUL2-RBX1 complexes were isolated and purified as described for $^{MBP/HIS}$FEM1B.

For the full CUL2, RBX1, ELONGIN B/C, FEM1B ligase complex (CUL2^{FEM1B}), the above purifications were performed in parallel until the dialysis step. Both imidazole elutions were mixed and diluted by a factor of 2 into 50mM HEPES 7.5, 150mM NaCl, 5mM β-mercaptoethanol, and 20% glycerol to 10% final and rocked for 1 h at 4°C. After the incubation, TEV protease was added at

1 μg:100 μg TEV to protein ratio to cleave MBP off FEM1B and the HIS tag off CUL2. Reactions were dialyzed in 50mM HEPES 7.5, 150mM NaCl, 1mM DTT, and 10% glycerol overnight. The sample was spun at 30,000 g for 30min and the supernatant loaded onto a MonoQ 10/100 anion exchange starting at 90% Buffer A (40mM HEPES 7.5, 1mM DTT, 10% Glycerol) and 10% buffer B (40mM HEPES 7.5, 1M NaCl, 1mM DTT, 10% Glycerol) increasing to 100% buffer B over 15 column volumes. Fractions corresponding to cleaved FEM1B-CUL2 complex were concentrated and run on a HiLoad 16/600 Superdex 200pg in 40mM HEPES 7.5, 150mM NaCl, 1mM DTT, 10% Glycerol and the complex fractions were concentrated, aliquoted, and flash frozen.

^{FLAG}FNIP1/^{HA}FLCN complexes were purified from 293Ts using affinity-purification, as described for immunoprecipitation mass spectrometry for Flag-FNIP1 FLCN complexes. 3xFLAG peptide elutions were treated with 1mM TCEP for 30min on ice and spun through Amicon Ultra 0.5ml centrifuge concentrator filter ultracel −30k NMWL (Sigma-Aldrich, UFC5030) to a final volume of 50-100μl. Fresh buffer (40mM HEPES 7.5, 150mM NaCl, 1mM TCEP) was then added and this centrifuge and buffer exchange step was repeated 3 times to remove detergent and 3xFlag peptide. After the last buffer exchange the Flag-FNIP1/HA-FLCN complexes were aliquoted and flash frozen.

E1/UBA1, UBE2R1, UBE2D3, and MBP-FBXL17 were purified previously described (Jin et al., 2012; Mena et al., 2018; Wickliffe et al., 2011). The GATOR1 complex was a generous gift from Roberto Zoncu (Lawrence et al., 2019). HALO-TUBES was purified as described for recombinant FEM1B. The neddylation machinery (human UBA3 (E1, E-313), UBE2M (E2, E2-656), NEDD8(UL-812)) and ubiquitin (U-100H) were purchased from Boston Biochem.

Seahorse analysis

C2C12 cells were seeded into XF^{e}96 Cell Culture Microplates (Agilent, 103729-100) at a density of 320 cells/well to 500 cells/well with no coating. 6-7 wells per condition were transfected with siRNAs and 36h analyzed post-transfection by a Seahorse XF analyzer. Seahorse XF Glycolytic rate and mitochondria stress tests were performed according to the manufacturers recommendation (Agilent, 103710-100 and 103015-100). For the mitochondria stress tests, 1.5μM oligomycin, 2μM FCCP, and 0.5μM Antimycin A/Rotenone final concentrations were used. All media changes were done using an Agilent Velocity 11 Bravo Automated Liquid Handling Platform. After the analysis, cells were fixed in 4% formaldehyde in PBS with Hoechst stain for 30 minutes, washed 3x in PBS, and imaged on an Opera Phenix automated microscope using a 20x objective to capture the entire well. The nuclei count was determine using the Perkin Elmer Harmony software and all data was normalized to the nuclei count of each well.

Immunofluorescence and confocal microscopy

C2C12 cells were seeded (10,000 cells/ml) on coverslips in 12 well plates. The next day cells were transfected with indicated siRNAs 15nM each siRNA (30nM final). 24h post transfection, media was changed on all plates. ~40h after transfection, cells were fixed in 4% formaldehyde in 1X PBS for 20min at room temperature, permeabilized with 0.1% Triton X-100 in 1X PBS, blocked in 10% FBS in 1X PBS, stained with 1° antibodies for 3h at room temperature, followed by staining with 2° antibodies and Hoechst stain. Samples were mounted onto coverslips and imaged using an Olympus IX81 microscope equipped with a Yokogawa CSU-1X confocal scanner unit (CSUX1 Borealis Square Upgrade Module), an Andor iXon3 camera (IXON DU-897-BV), and an Andor Technology Laser Combiner System 500 series equipped with four laser lines. Images were analyzed using Metamorph Advanced (Molecular Devices) and Fiji (Schindelin et al., 2012).

NAD/H NADP/H measurements

C2C12 cells were seeded into 6cm plates (100,000 cells) and transfected the day after with siRNAs. 36h after transfection, the media was changed on all plates. NAD+/H and NADP+/H were measured from the same cells using NAD/NADH-Glo and NADP/NADPH-Glo Assays (Promega, G9071 and G9081). To measure both reduced and oxidized forms cells were washed one time with PBS and lysed in 1:1 PBS and 0.2N NaOH 1% dodecyltrimethylammonium bromide. Lysates were split into three tubes: one for protein normalization, one as a base treated (left unmodified, NADH/PH detection) and the last as acid treated (0.4 N HCl acid added, NAD/P detection). The base and acid treated samples were heated to 60°C for 15min, cooled and neutralized. Samples were then split and processed for NAD and NADP quantifications on a Perkin-Elmer Envision Multilabel Plate Reader. Data was normalized using protein concentration of lysates.

H_2O_2 measurements

C2C12 cells (20k cell/well) were seeded into 12 well plates. Cells were transfected the next day with indicated siRNAs (30nM final). 24h after transfection, the media was changed on all wells. 36h after transfection, H_2O_2 was measured using the ROS-Glo H2O2 Assay (Promega, G8820) according the manufactures protocol in growth media using Perkin-Elmer Envision Multilabel Plate Reader to measure luminescence. After the media was removed for the assay, cells were lysed in their wells with (40mM HEPES 7.2, 150mM NaCl, 0.2% NP40) on ice. Lysates were cleared with 21000 g spin at 4°C for 10min and the supernatants' A_{280} was measured to determine protein concentrations for normalization. For 293T experiments, 140k cell/well were seeded into 12 well plates. The next day, cells were treated with DMSO, 250nM Antimycin A or 250nM Myxothiazol (Sigma-Aldrich, A8674 and T5580). 16 hours later H_2O_2 was measured as described above.

^{13}C labeling

C2C12 myoblast were seeded into either 10 or 6 cm plates at 250k cell/plate or 100k cell/plate respectively 5 plates per condition. The next day, cells were transfected with siRNAs (30nM final, single depletions had siCNTRL added to 30nM final). 24h after transfection, media was changed on all plates. 36h post transfection, cells were rinsed once in 3ml –glucose media (DMEM –glucose, 4mM glutamine, 10% dialyzed fetal bovine serum) and cells incubated in 4ml –glucose media supplemented with 5mM ^{13}C glucose (Sigma-Aldrich, 389374) for 4h to reach steady state labeling. After incubation, cells were washed in ice cold 0.1M ammonium bicarbonate and 500 μL of extraction buffer (methanol: acetonitrile: water = 40:40:20 with 0.1 M formic acid) containing 1 μM of isotopic AMP (Sigma-Aldrich, 900382) and Fructose-1,6-bisphosphate (Cambridge Isotope Laboratories, Inc., CLM-6678-0) as standards, respectively was added to each plate. Plates were gently shaken for 10sec, scraped, and transferred to tubes on ice for 15min. Samples were centrifuged at 21000 g for 10min at 4°C. 180μl of supernatant was added to 20 μL of 1M ammonium bicarbonate, mixed, and flash frozen in liquid nitrogen.

LC/MS-based analyses of glycolytic and TCA intermediates were performed on liquid chromatography system (LC; 1200 series, Agilent Technologies) connected in line with an LTQ-Orbitrap-XL mass spectrometer equipped with an electrospray ionization (ESI) source (Thermo Fisher Scientific) at the UC Berkeley QB3/Chemistry Mass Spectrometry Facility. 20μl of each metabolite sample was injected onto a ZIC-pHILIC 2.1 X 150 mm (5 μm particle size) column (EMD Millipore). Buffer A was 20 mM ammonium carbonate, 0.1% ammonium hydroxide; buffer B was acetonitrile (Optima LC-MS grade, Fisher Chemical). The chromatographic gradient was run at a flow rate of 0.2 ml/min as follows: 0-20 min: linear gradient from 80% to 20% B; 20-20.5 min: linear gradient from 20% to 80% B; 20.5-35 min: hold at 80% B. The mass spectrometer was operated in the negative ion mode and column temperature was 25°C. Mass spectra were recorded over the range of 70-1000 mass-to-charge ratio (m/z). Metabolite identification and quantification were performed using Xcalibur software (version 2.0.7, Thermo Fisher Scientific).

TUBE binding

For endogenous detection of FNIP1 ubiquitylation, 1 15 cm plate of 293T cells was treated overnight (~16h) with either DMSO, 350nM, or 500nM of Bardoxolone methyl (Sigma-Aldrich, SMB00376), and 500nM MLN4924 (Cayman Chemical, 15217) as indicated. All samples were also treated with 2 μM Carfilzomib (Selleck Chemical, PR-171) for 4h prior to harvesting. Cells were scraped in cold PBS, spun down, and frozen in liquid nitrogen. Cell pellets were lysed, cleared, and normalized as described small-scale immunoprecipitation but with 500 μL modified lysis buffer (40mM HEPES 7.2, 150mM NaCl, 10mM N-Ethylmaleimide, 0.1mM TCEP, 1% Triton and with or without 3 μM HALO-TUBES). Normalized lysates were added to HALO-link resin (Promega, G1914) and rocked for 1-2 hours at 4°C. Beads were washed 4x in Lysis buffer without NEM and eluted with 2x urea sample buffer. pET28a-6HIS_TEV-HALO-4x ubiquilin UBA TUBE (DU23799) was obtained through the MRC PPU Reagents and Services facility (MRC PPU, College of Life Sciences, University of Dundee, Scotland; mrcppureagents.dundee.ac.uk).

Glucose uptake assay

C2C12 cells were seeded into 96 well white cell culture microplate plate at 320 cell/well and transfected with indicated siRNAs the next day (8 wells per condition). Additional 50 μL of media was added to each well the night before the assay and ~40h after siRNA transfection 4 wells per condition were analyzed using the Glucose Uptake-Glo Assay (Promega, J1341) following manufacturer's recommendation with a 10min 2-deoxyglucose incubation. 4 control wells were not incubated with 2DG as a background control. The remaining 4 wells were fixed in 4% formaldehyde in PBS with Hoechst 33342 (AnaSpec, 83218) for 30min, washed 3x in PBS, and imaged on an Opera Phenix automated microscope using a 20x objective to capture the entire well. The nuclei count was determine using the Perkin Elmer Harmony software and was used to normalize the data to the average number of cells/well for each treatment.

Mitosox staining

C2C12 were siRNA transfected and differentiated as described for myotube analysis. At Day 3 of differentiation the media was removed and 5 μM MitoSox (Invitrogen, M36008) in Hank's balanced salt solution (HBSS) was added for 10 min at 37°C with 5% CO_2. Cells were washed 3 times with HBSS and imaged using an Opera Phenix automated microscope at 37°C with 5% CO_2.

Antibodies

The following antibodies were used in this study: anti-Flag (Clone M2, Sigma-Aldrich, F1804), anti-CUL2 (Bethyl, A302-476A), anti-FNIP1 (Abcam, ab134969), anti-FNIP1 (Abcam, 215725), anti-GFP (Abcam, ab6556), anti-FEM1B (Proteintech, 19544-1-AP), anti-MYOSIN, SARCOMERE (MHC) (Developmental Studies Hybridoma Bank, M20), anti-MYOGENIN (Developmental Studies Hybridoma Bank, F5D) anti-beta-ACTIN (MP Biomedicals, clone C4, 691001), α-TOMM20 (Sigma-Aldrich, HPA011562), anti-HA-Tag (C29F4, Cell Signaling Technology (CST), 3724), anti-Flag DYKDDDDK Tag (CST, 2368), anti-FLCN (D14G9, CST, 3697), anti-KEAP1 (D6B12, CST, 8047), anti-NRF2 (D1Z9C, CST, 12721), anti-CITRATE SYNTHASE (D7V8B, CST, 14309), anti-GAPDH (D16H11, CST, 5174), anti-Phospho-AMPKα (Thr172) (40H9, CST, 2535), anti-AMPKα (D5A2, CST, 5831), anti-Phospho-p70 S6 KINASE (Thr389) (108D2, CST, 9234), anti-p70 S6 KINASE (49D7, CST, 2708), anti-Phospho-Acetyl-CoA CARBOXYLASE (Ser79) (CST, 3661), and anti-Acetyl-CoA CARBOXYLASE (C83B10, CST, 3676).

Cloning

Fem1b, Nprl2, Fnip1, Fnip2, Flcn, Rbx1, Elongin B, Elongin C, Cul2, constructs were cloned from cDNA prepared from C2C12s. DEPDC5, NPRL3, and TRX were generated from 293T cDNA. We cloned FNIP1 as two isoforms, full length and a truncation missing 208-235. Both isoforms interact with and are degraded by Fem1b, but the short form of FNIP1 expresses considerably better and retains binding to currently known FNIP1 interactors. All FNIP1 experiments presented in this study use the short isoform and the residue positions indicated are reference to this isoform. All FEM1B and FNIP1 mutants were generated by overlap extension polymerase chain reaction, or site directed mutagenesis using quick change method. The pCS2+-GFP-degron-IRES-mCherry reporter was generated using Gibson assembly of all of the individual components (GFP, IRES, mCherry, and pCS2) (Gibson et al., 2009). A 4xGly-Ser linker was added between GFP and two Esp3I sites (NEB, R0734S) which allow for the easy insertion of DNA fragments. The FNIP1 degron was inserted into the reporter construct by annealing and phosphorylating two oligos corresponding to degron sequences with the forward oligo containing an extra CAGC at the 5′ end and the reverse oligo with 5′- ATCA, each complementary to overhangs generated by the Esp3I digest.

shRNA production and viral production

All lentiviral constructs were cloned and transformed into Stbl3 E. Coli (Thermo Fisher Scientific, C737303). Lentiviral shFEM1B pLKO.1 constructs were purchased from Sigma-Aldrich (shFEM1B$^{\#1}$: TRCN0000303677125, shFEM1B$^{\#2}$: TRCN0000299671125, shFEM1B$^{\#3}$: TRCN0000303647125, shFEM1B$^{\#4}$: TRCN0000303746125, shTXNRD1: TRCN0000046535, shGSR: TRCN0000046425). pLenti-PGK-Hygro-Flag-CUL2 and shRNA containing Lentiviruses were generated in 293T cells by co-transfection with lentiviral constructs with packaging plasmids (pMD2.5G Addgene, 12259; psPAX2 Addgene, 12260) using PEI. Viral supernatants were collected and filtered through a 0.45μm filter and concentrated with LentiX concentrator following the manufactures protocol (Takara 631232). Precipitated virus was resuspended in media, aliquoted, and frozen.

Quantitative real time PCR analysis

Total RNA from C2C12 cells myoblasts grown in 6cm dishes and was purified using nucleospin RNA kit (Macherey-Nagel, 740955). cDNA was generated (Thermo Fisher Scientific, F470) and qRT-PCRs were performed on a StepOnePlus Real-Time PCR System (Applied Biosystems) using 2X KAPA SYBR FAST qPCR Master Mix (Roche, KK4602). All qPCR primers were ordered from IDT and sequences can be found in Table S3.

Immunoprecipitation and mass spectrometry

Large scale immunoprecipitations were performed after harvesting cells in cold PBS (20 15cm plates of transfected C2C12 cells or 10 15cm plates of 293T cells) and centrifuging them at 300 g for 10min, and flash freezing them in liquid nitrogen. Cell pellets were re-suspended in 5x the volume of pellet weight (ml/g) of lysis buffer (40mM HEPES 7.5, 150mM NaCl, 0.2% NP40, with Roche cOmplete Protease Inhibitor Cocktail, the ^{FLAG}FNIP1 IP lysis buffer also contained 10mM β-glycerol phosphate, 10mM sodium pyrophosphate, 2.5mM $MgCl_2$). CUL3 and ^{Flag}CUL2 IP lysis buffer contained 2mM 1,10-Phenanthroline (Sigma-Aldrich, P1,280-4). Lysates were gently rocked for 1h at 4°C and cleared by centrifugation at 500 g, 5min and 21000 g, 30min. Supernatants were added to 90 μL of ANTI-FLAG® M2 Affinity Agarose Gel slurry (Sigma-Aldrich, A2220) and rotated for 1-2h at 4°C. Beads were washed extensively in lysis buffer and eluted 2x with 250 μL of 3xFlag peptide (F4799, Millipore). Elutions were pooled and precipitated overnight on ice with 20% trichloroacetic acid. The precipitated pellets were washed in acetone, dried, and solubilized in 8M urea, 100mM TRIS, pH 8.5. The samples were reduced with TCEP, alkylated with iodoacetamide, and digested overnight with trypsin (V5111, Promega). Trypsinized samples were analyzed by Multidimensional Protein Identification Technology (MudPIT) at the Vincent J. Coates Proteomics/Mass Spectrometry Laboratory at UC Berkeley. Specific proteins were identified by comparing each IP to a dataset of 40-150 similar (databases for C2C12 and 293T cells) αFLAG IP/mass spectrometry samples using CompPASS analysis (Huttlin et al., 2015). All total spectral counts were normalized to TSC of bait (4000 for all experiments except for CUL3 and CUL2 C2C12 analysis).

Genome editing

FEM1B knockout HEK293T cell lines were generated using the ribonucleoprotein (RNP) method (DeWitt et al., 2017) using guides targeting the 5′ UTR and intronic regions adjacent to exon1 of FEM1B (5′-ATTAACGAGTCCGCGCGCGT-3′, 5′-AAGAC GAGCTTTCGCAGACA-3′). Guide RNAs were synthesized with NEB HiScribe T7 High Yield RNA Synthesis Kit (E2040S), DNase treated with turboDNase (Thermo Fisher Scientific, AM2238), and purified with a MEGAclear clean-up kit (Thermo Fisher Scientific, AM1908). RNPs were assembled with Cas9 purified by the UC Berkeley QB3 MacroLab in a 10 μL reaction of 100 pmol of Cas9 and 120 pmol sgRNA in Cas9 buffer (20 mM HEPES 7.5, 150 mM KCl, 10% glycerol, 1 mM TCEP). Reactions were gently mixed for 30 s and incubated for 20min at room temperature. RNP complexes and 200k 293T cells resuspended in buffer SF (Lonza) were added to a nucleofection strip and the mixture pulsed with program DS150 Lonza 4D-Nucleofector. Cells were plated into 6 well dishes. Endogenous ^{3xFLAG}FEM1B 293T cell lines were generated using a guide targeting near the start codon of FEM1B (5′-GGCGGCGGCCATGGAGGGCC-3′) that was cloned into pX330 and cotransfectd with a 200bp repair template containing a 3xFLAG tag (5′-TCCGGGGGCGCACGGCAGCTGCAGCGGTGGCGACCAAACGGGTGTTGGAGTTGGCGGCGGCCATGGACTACAAAGAC CATGACGGTGATTATAAAGATCATGACATCGATTACAAGGATGACGATGACAAGGAGGGCCTGGCTGGCTATGTATACAAGGCGG CCAGCGAGGGCAAGGTGCTGACTCTGGCCGCCTTGCTT-3′) using Lipofectamine 2000 (Thermo Fisher Scientific, 11668019).

After confirmation of bulk editing by PCR for both knockouts and knock-ins, cells were diluted to 5cells/ml and 100 μL of cell suspension was plated per well plated into 96 well plates containing 200 μL total media, 20% FBS DMEM + Pen/Strep. Colonies were expanded and screened for homozygous knockout or 3xFLAG tagging by PCR and western blot and confirmed by DNA sequencing.

NGS Library Prep and RNA-seq

Total RNA was extracted from sub-confluent C2C12s treated with siFEM1B, siKEAP1, siFEM1B-siKEAP1, or siCNTRL siRNAs (in triplicate) using a NucleoSpin RNA mini kit (Macherey-Nagel, 740955.250). NGS libraries were made using a TruSeq Stranded Total RNA kit (Illumina), with an average size of 250 bp. Libraries were prepared by the UC Berkeley Functional Genomics Laboratory. Paired-end RNA-sequencing was done using a HiSeq400 (Illumina). Sequencing of the libraries was done two times to obtain technical replicates.

RNA-seq Alignment, Expression Analysis and Transcription Factor Enrichment

We used the Kallisto-Sleuth pipeline to perform differential gene expression analysis between samples (Pimentel et al., 2017). Briefly, paired-end RNA-seq reads were aligned using Kallisto, using the mm10 *Mus musculus* reference transcriptome and 200 bootstrap steps. For differential expression analysis, the R Sleuth package was used. To obtain log2 fold changes, we had to implement the following transformation function during the initial sleuth object (so) preparation step:

$$so <- sleuth\_prep(s2c, \sim condition / bio\_samp, extra\_bootstrap\_summary = TRUE, target\_mapping = t2g, transformation\_function = function(x) log2(x + 0.5))$$

To identify significant differentially expressed genes, the following conditions were compared: siCNTRL v siFem1b; siCNTRL v siKeap1; siFem1b v siKeap1. From each comparison, significant differentially expressed genes with a qval $\leq$ 0.075 were kept. This generated four different gene lists, which were then merged together. This gene list was used to generate heatmaps for data visualization. Heatmaps of significant differentially expressed genes were generated using the R "heatmap.2" package, normalized by row, and using unsupervised clustering applying the "ward.D2" option. Transcription factor enrichment for significant differentially expressed genes was done using the ChEA3 and oPOSSUM algorithms (Keenan et al., 2019; Kwon et al., 2012).

Transmission electron microscopy

siCNTRL, siFEM1B, siFNIP1, and siFNIP1-siFEM1B treated C2C12 cells were grown to 50% confluence and fixed in 2% guleteraldehyde: 0.1 M sodium cacodylate (pH 7.2) for 20 min, followed by 3 washes with 0.1 M sodium cacodylate buffer. Cells were then gently harvested and collected in 1.5 mL Eppendorf tubes, followed by imbedding in agarose plugs. After solidifying, agar plugs containing the specimens were carefully cut into ~2.5 mm^3 slices. Slices were stained in 1% osmium tetroxide in 0.1 M sodium cacodylate for 1 hr, followed by 1.38% potassium ferricyanide for 1 hr. Stained samples were step-dehydrated in acetone (35%, 50%, 70%, 80%, 95%, 100%, 100%) for 10 min at each step. Dehydrated samples were then step-infiltrated with acetone:Epon resin (2:1, 1:1, 1:2 for 1 hr each). After final acetone:resin infiltration, samples were embedded in pure Epon resin at room temperature, overnight, followed by curing at 65°C for two days. Cured samples were then sliced using a Leica UC 6 microtome, taking 70 nm sections. Sliced sections were picked up on 100 mesh formvar-coated copper grids, then stained with 2% aqueous uranyl acetate for 5 min, followed by 2% lead citrate for 2 min. Grids were examined under a Tecnai 12 TEM at 120 kV.

QUANTIFICATION AND STATISTICAL ANALYSIS

All quantifications are presented as the means ± standard deviation. Significance was determined by 2 tailed t test, *p < 0.05; **p < 0.01; ***p < 0.001. All quantitative myotube analysis figures represent at least 3 independent biological replicates (Figure 1A is 2 biological replicate screen done in duplicate and Figure S2J are the quantification of 2 technical replicates). Seahorse and glucose uptake quantification in Figures 7A, 7B, and 7E is presented as the mean of 4-6 wells per condition. ECAR measurements were calculated from 4 biological replicates consisting of 5-6 well each. All luciferase assays were measured from 5 biological replicates unless otherwise indicated (Figure 1E comprises 2 biological replicates Figure S5D is from 1). All metabolomics experiments are quantified from 5 technical replicates. For the NRF2 nuclear localization ratio a mask was created in Fiji for the nuclei channel (Hoechst) and for the cytoplasm 1 μm around the nuclei mask, the NRF2 signal from these masks was measured (n = 15-20). For the mitochondrial distance measurement, a line was drawn from the edge of nuclei to the farthest point of the mitochondrial staining (n = 10-15, **p = 9.05E-11 and ***p = 1.57E-12).

Supplemental Figures

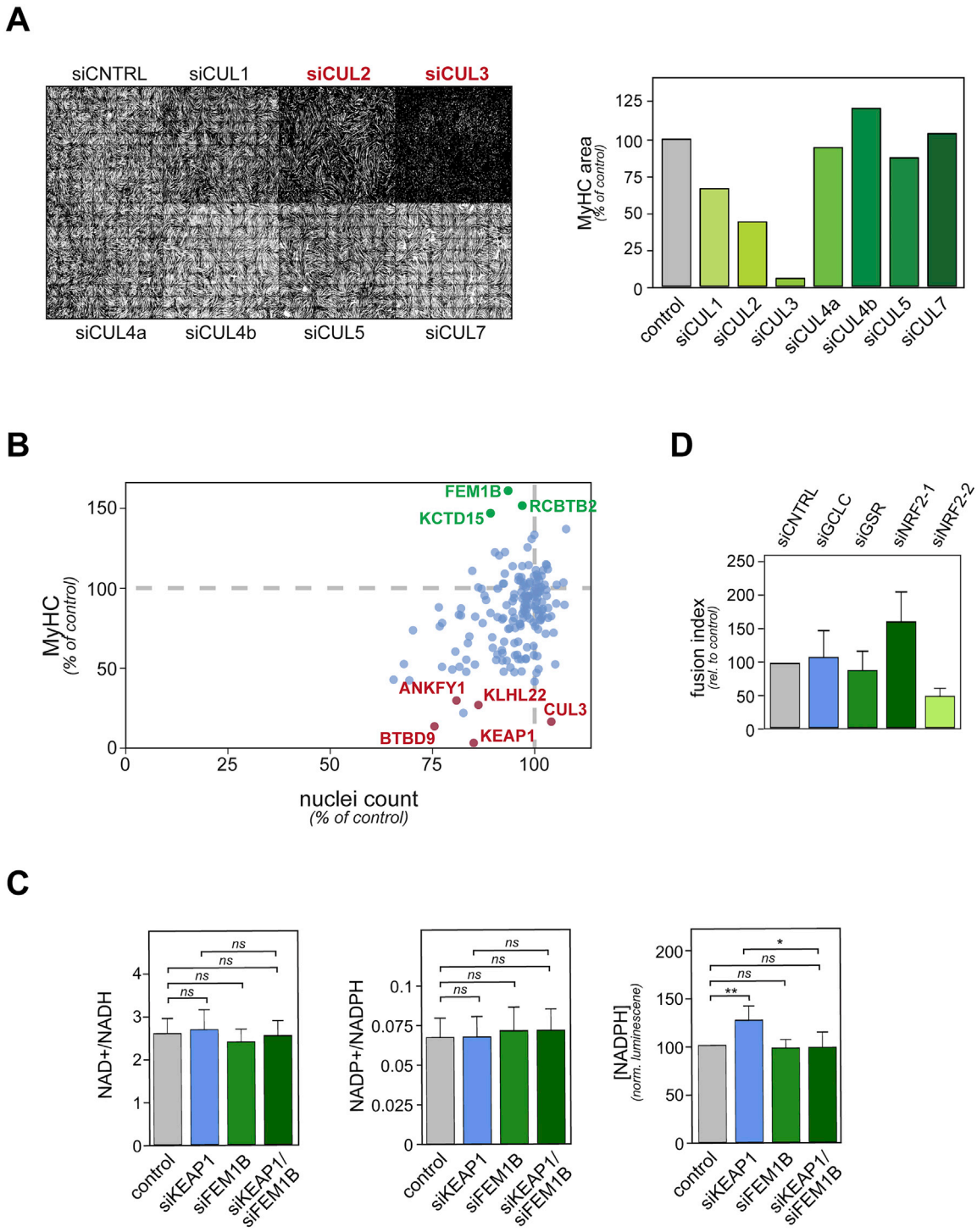

Figure S1. CRL2 and CRL3 E3 Ligases Are Required for Myoblast Differentiation, Related to Figure 1

A. CUL2 and CUL3 are required for myotube differentiation. C2C12 myoblasts were depleted of CUL1, CUL2, CUL3, CUL4a, CUL4a, CUL5, and CUL7, differentiation was induced, and formation of myotubes was followed by automated microscopy against MyHC. Quantification is shown on the right with

(legend continued on next page)

mean ± SEM B. CRL adaptors affect myotube formation independently of effects on cell division or survival. C2C12 myoblasts were depleted of the indicated CRL2- or CRL3-adaptors and subjected to differentiation. Nuclei were stained by Hoechst and counted by automated image analysis. C. NAD^+/NADH ratio, $NADP^+$/NADPH ratio, and total NADP/NADPH levels from C2C12 myoblasts depleted of KEAP1, FEM1B, or both. Quantification of five biological replicates with mean ± SEM D. C2C12 cells were depleted of GCLC, GSR, NRF2 (using two siRNA sequences). Myotube formation was quantified after immunofluorescence microscopy against MyHC, using at least 4 biological replicates with mean ± SEM.

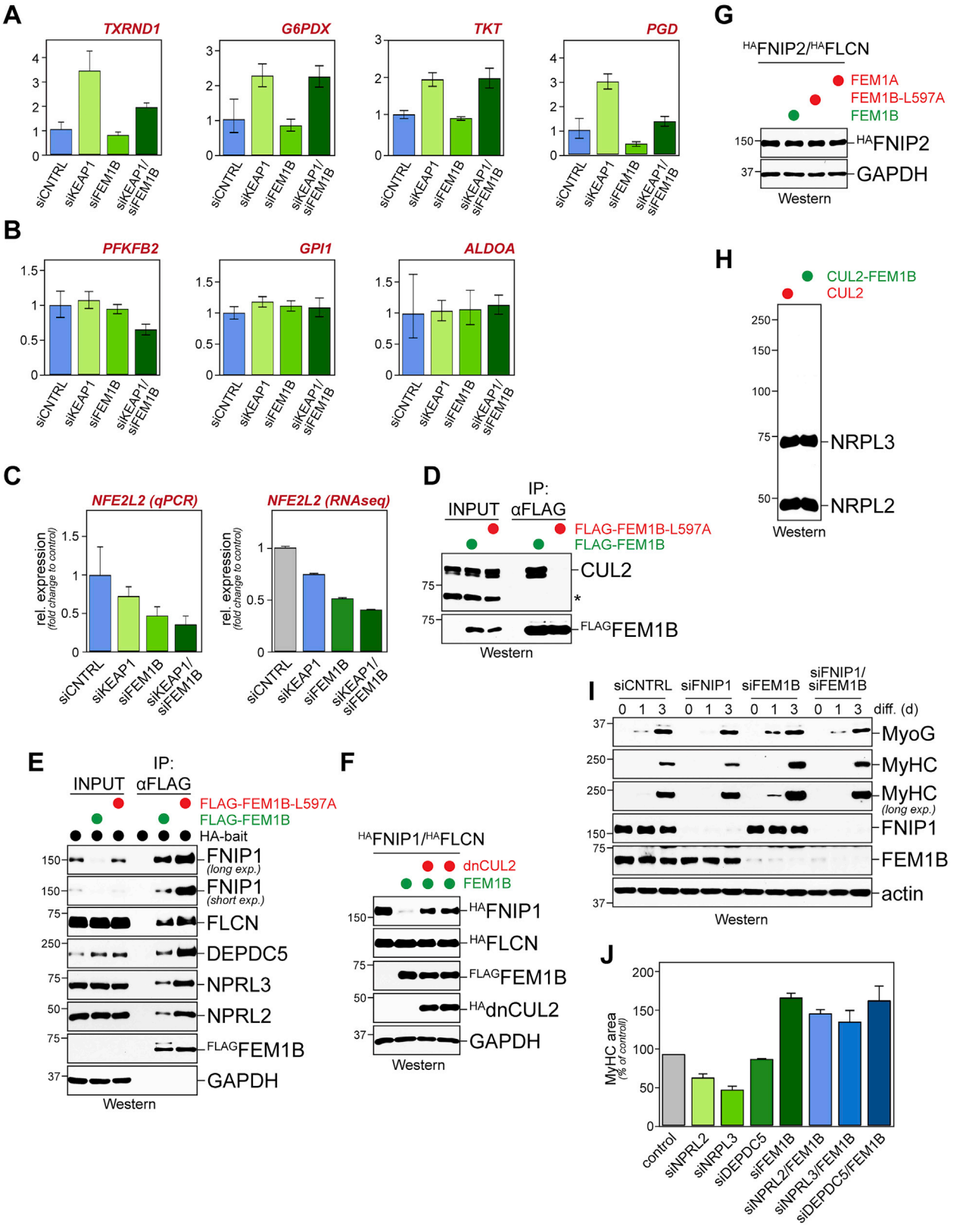

(legend on next page)

Figure S2. FNIP1 Is a Specific Substrate of CUL2^{FEM1B}, Related to Figure 3

A. qRT-PCR of select pentose phosphate pathway NRF2 target genes in C2C12 myoblasts depleted of KEAP1, FEM1B, or both with mean ± SEM B. qRT-PCR of putative NRF2 glycolysis target genes in C2C12 myoblasts depleted of KEAP1, FEM1B, or both with mean ± SEM C. NFE2L2 (NRF2) expression measured by qRT-PCR and RNaseq from myoblasts depleted of KEAP1, FEM1B, or both with mean ± SEM D. FEM1B^{L597A} does not bind CUL2. ^{FLAG}FEM1B or ^{FLAG}FEM1B^{L597A} were affinity-purified from 293T cells and bound CUL2 was detected by western blotting. E. FEM1B^{L597A} shows enhanced binding to FNIP1, FLCN, and GATOR1 subunits. ^{FLAG}FEM1B or ^{FLAG}FEM1B^{L597A} were affinity-purified from 293T cells that also expressed ^{HA}FNIP1, ^{HA}FLCN, or HA-tagged GATOR1 subunits. Binding of HA-tagged proteins to FEM1B was detected after αFLAG affinity-purification by gel electrophoresis and western blotting using αHA antibodies. F. CUL2 activity is required for FEM1B-dependent degradation of FNIP1. Cells were transfected with ^{FLAG}FEM1B, ^{HA}FNIP1, ^{HA}FLCN, and dominant-negative ^{HA}dnCUL2 (1-427), as indicated, and FNIP1 abundance was determined by western blotting. G. FEM1B does not induce the degradation of FNIP2, a close homolog of FNIP1. Cells were transfected with ^{HA}FNIP2 and the indicated FEM1B constructs, and FNIP2 levels were determined by gel electrophoresis and western blotting using αHA antibodies. H. CUL2^{FEM1B} does not ubiquitylate GATOR1. DEPDC5, ^{FLAG}NPRL2 and ^{FLAG}NPRL3 were purified from insect cells, incubated with recombinant CUL2 or CUL2^{FEM1B}, ATP, E1, UBE2D3 and UBE2R1 as E2s, and ubiquitin, and analyzed for ubiquitylation by gel electrophoresis and western blotting. I. C2C12 cells were depleted of FEM1B, FNIP1, or both, and differentiation was induced as described. The differentiation efficiency was monitored by western blotting against MYOG and MyHC. J. Co-depletion of NPRL2, NPRL3, or DEPDC5 does not rescue the increased myogenesis seen in cells lacking FEM1B. C2C12 myoblasts were transfected with the indicated siRNAs, induced to differentiate, and analyzed by microscopy against MyHC.

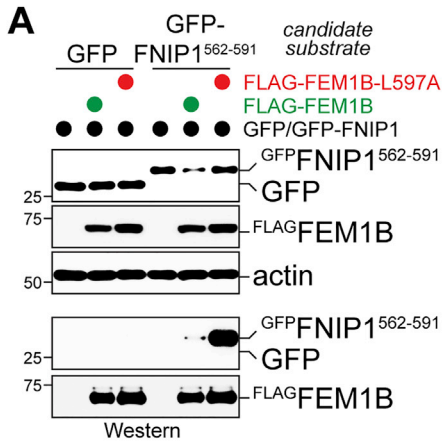

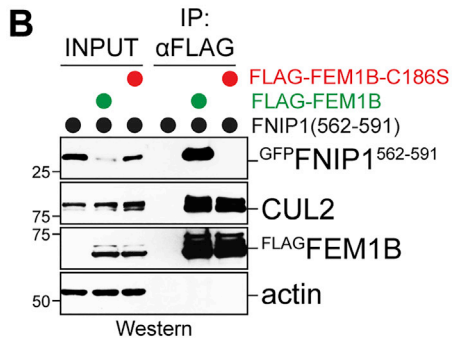

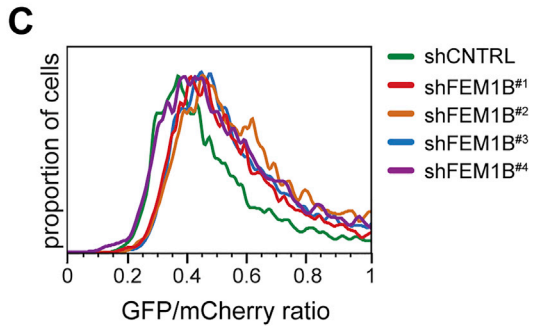

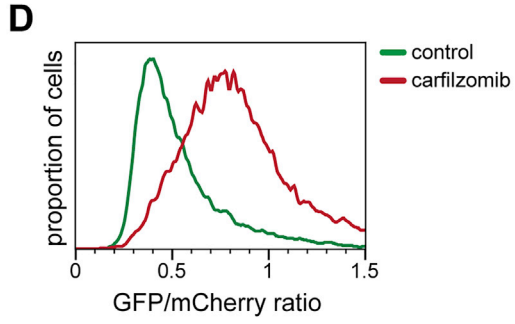

E

Mouse	SEETRTPN**C**N**C**KY**C**SHPVLG
Hamster	SEETRTPNCNCKYCSHPLLG
American beaver	SEETRTPNCNCKYCTHPLLG
Mongolian gerbil	SEEIRTPNCNCKYCSHPLLG
Gorilla	SEEIRTPNCNCKYCSHPLLG
Homo sapiens	SEEIRTPNCNCKYCSHPLLG
Ground squirrel	SEETRTSNCNCKYCSHPLLG
Cow	SEETRTPNCNCKYCSRPLLG
Horse	SEETRTPNCNCKYCSRPLLG
Chinchilla	SEETKTPHCNCKYCSHPLLG
Cat	-EETRTPNCNCKYCSRPLLG
Dog	-EETRTPNCNCKYCSRPLLG
Macaca	SEEIRTPSCNCKYCSHPLLG
Chinese hamster	SEEIRTPNCNCKYCSHPLLG
Microtus ochrogaster	SEETRTPSCNCKYCSHPLLG
Meriones unguiculatus	SEEIRTPNCNCKYCSHPLLG
Myotis davidii	SEETRTPNCNCKYCSHPLFG
Ictidomys tridecemlineatus	SEETRTSNCNCKYCSHPLLG
Urocitellus parryii	SEETRTSNCNCKYCSHPLLG
Myotis lucifugus	SEETRTPNCNCKYCSHPLFG
Pteropus Alecto	SEEMRTPNCNCKYCSHPLLG
Equus przewalskii	SEETRTPNCNCKYCSRPLLG
Tupaia chinensis	SEETRTPNCNCKYCSRPLLG
Hipposideros armiger	SEETRTPNCNCKYCSRPLLG
Camelus ferus	SEETRTPNCNCKYCSPPLLG
Chinchilla lanigera	SEETKTPHCNCKYCSHPLLG
Rhinopithecus bieti	SEEIRTPSCNCKYCSHPLLG
Macaca fascicularis	SEEIRTPSCNCKYCSHPLLG
Tursiops truncates	SEETRTPNCSCKYCSRPLLG
Propithecus coquereli	SEETRTPNCNCKYCGRPLLG
Marmota monax	SKETRTSNCNCKYCSHPLLG
Miniopterus natalensis	SEETRTPNCNCKYCSPALLG
Octodon degus	SEETKAPHCNCKYCSHPLLG
Rattus norvegicus	SEETGTSNCNCKYCSHPLLG
Heterocephalus glaber	SEETKTPHCNCKYCIHPLLG
Cavia porcellus	SEETKIPHCNCKYCNHPLLG
Oryctolagus cuniculus	SEETRTPNCGCKYCTRPLVG
Chelonia mydas	SEEMRTPNCSCKYCKCPLLG
Python bivittatus	SEEVRTSDCSCKYCKCPV
Chaetura pelagica	SEEVRTSNCSCRYCKCPV
Notechis scutatus	SEEVRTSDCGCKYCRCPV
Cyanistes caeruleus	SEEMRVSNCSCKYCKCPV
Protobothrops mucrosquamatus	SEELRTSDCSCKHCKCPV
consensus	**E.(R/K)...C.C(R/K)YC..**

F

```
FNIP1 (mouse)        SEETRTPNCNCKYCSHPVLG
FNIP2 (mouse)        TAERRSPEPTVV--AEISEG

consensus            : * *:*:  .   :.   *
```

Figure S3. FNIP1 Contains a Conserved Degron for Recognition by CUL2^{FEM1B}, Related to Figure 4

A. The FNIP1 degron is sufficient to mediate binding to FEM1B. 293T cells were co-transfected with ^{FLAG}FEM1B or ^{FLAG}FEM1B^{L597A} and GFP or GFP^{degron} (GFP-FNIP1$^{562-591}$), as indicated. ^{FLAG}FEM1B variants were affinity-purified, and bound GFP was detected by western blotting. B. Degron binding to FEM1B is specific. ^{FLAG}FEM1B or the ankyrin mutant ^{FLAG}FEM1B^{C186S} were co-transfected with GFP^{degron}. ^{FLAG}FEM1B variants were affinity-purified, and bound GFP was detected by western blotting. C. Depletion of FEM1B by four independent shRNAs stabilizes the GFP-degron fusion, as observed after co-expression of GFP^{degron} and

(legend continued on next page)

mCherry and analysis by flow cytometry. D. Proteasome inhibition with carfilzomib stabilizes the GFP^{degron} reporter, as determined by flow cytometry. E. The Cys residues of the FNIP1 degron are invariant among FNIP1 homologs. F. The FNIP1 degron is not conserved in FNIP2, a protein otherwise highly similar to FNIP1. FNIP2 is not recognized by $CUL2^{FEM1B}$.

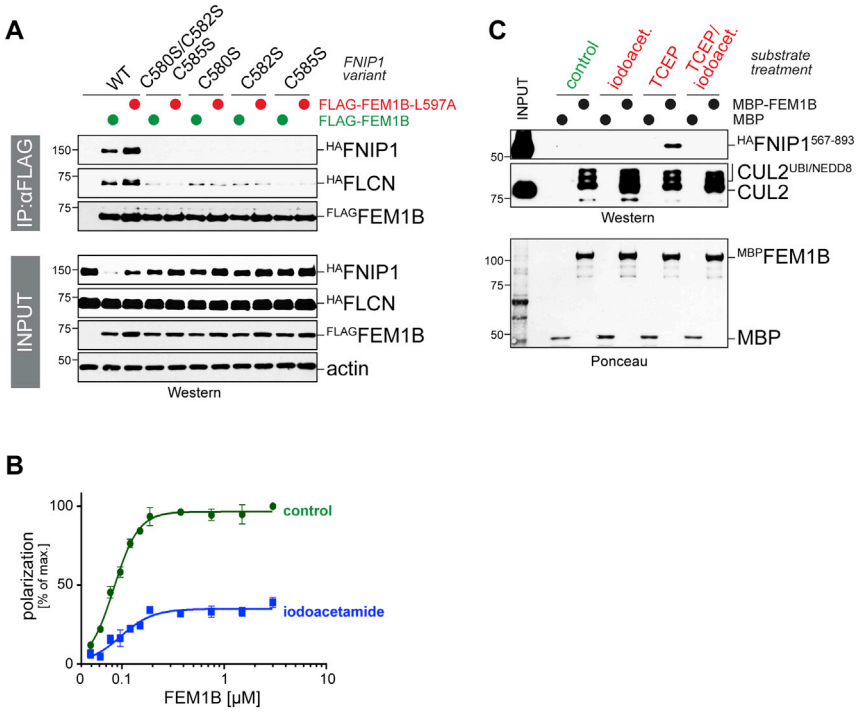

Figure S4. Cysteine Residues Are Essential for FNIP1 Degron Function, Related to Figure 5

A. Cys residues are essential for FNIP1 degron function, as seen by western blotting. HA-tagged FNIP1 variants were co-expressed with FLCN and FLAG-tagged FEM1B or FEM1B^{L597A}. FEM1B variants were immunoprecipitated and co-purifying FNIP1 was detected by gel electrophoresis and αHA-Western. B. Modification of degron Cys residues prevents binding to FEM1B. A TAMRA-labeled FNIP1 degron peptide was incubated with buffer (green) or iodoacetamide (blue). Binding to recombinant FEM1B was monitored by fluorescence polarization with mean ± SEM C. Reversible oxidation controls degron recognition by FEM1B. A rabbit reticulocyte lysate generated HA-tagged FNIP1 fragment containing the degron was incubated with recombinant ^{MBP}FEM1B. Reducing agent (TCEP) or a Cys-reactive modifier (iodoacetamide) were added as indicated. ^{MBP}FEM1B was purified on maltose agarose and bound FNIP1 or rabbit CUL2 were detected by western blotting.

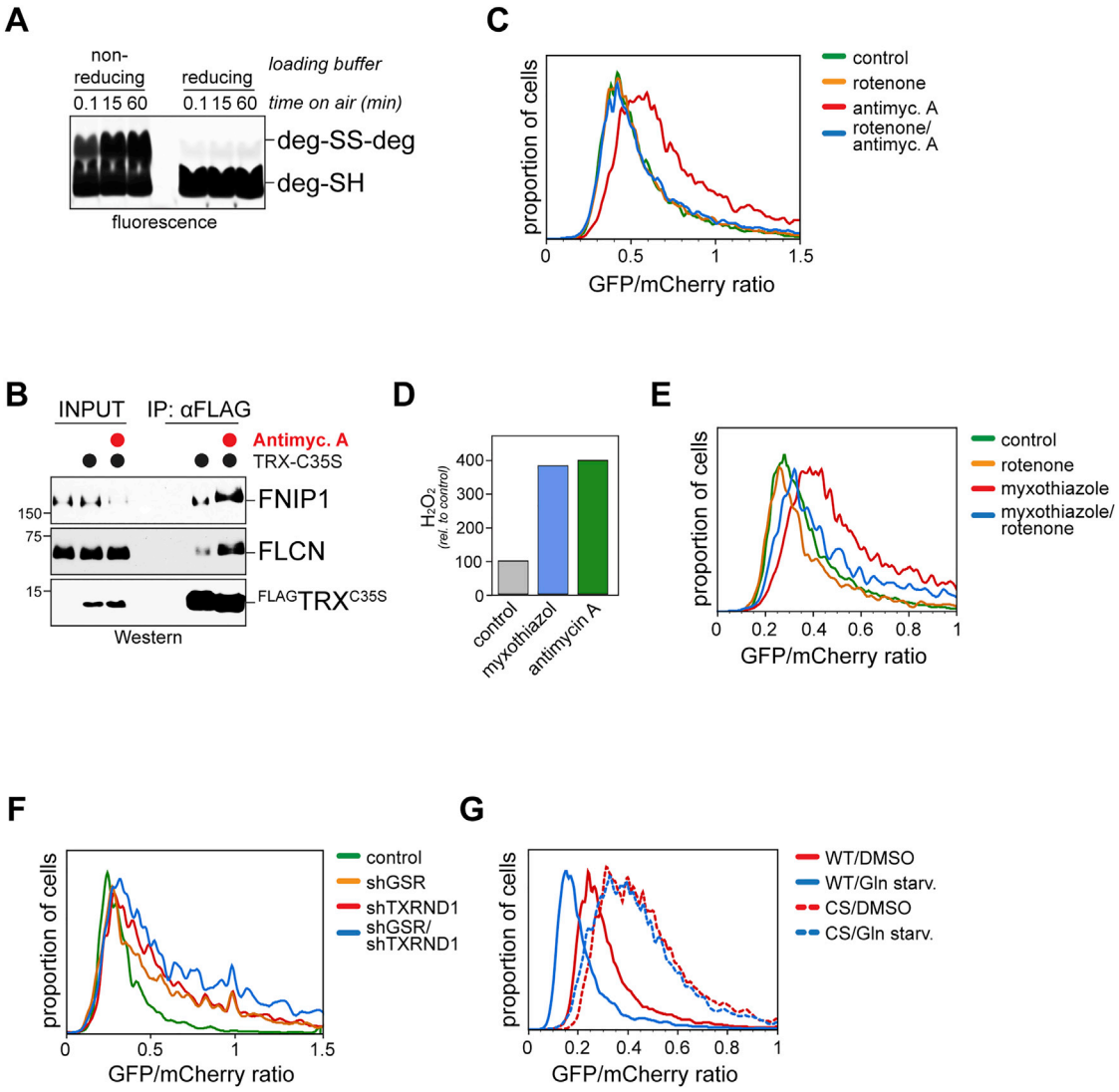

Figure S5. FEM1B Recognizes an Unmodified FNIP1 Degron, Related to Figure 6

A. The FNIP1 degron peptide rapidly forms disulfide bonds in solution. ^{TAMRA}FNIP1 degron peptide was diluted into buffer containing no reducing agent and aliquots were taken at indicated time points and added to sample buffer with or without reducing agent. Samples were analyzed by gel electrophoresis and fluorescence detection. B. The FNIP1 degron is oxidized in cells in the context of full-length FNIP1. TRX$^{C35S/FLAG}$ was affinity-purified from cells treated with antimycin A, and co-eluting endogenous FNIP1 and FLCN were detected by western blotting. C. Stabilization of the FNIP1 degron reporter by antimycin A is dependent on the activity of the electron transfer chain. Cells were either treated with antimycin A, rotenone (which inhibits electron delivery to complex III), or both, and the stability of GFP^{degron} was monitored by flow cytometry. D. Antimycin A and myxothiazol increase ROS production, as measured by a H_2O_2 detecting luciferase assay showing mean ± SEM E. Myxothiazol stabilizes the FNIP1 degron reporter. Cells were either treated with myxothiazol, rotenone, or both, and the stability of GFP^{degron} was monitored by flow cytometry. F. Depletion of thioredoxin reductase and glutathione reductase stabilize the FNIP1 degron reporter. 293T Cells were depleted of GSR, TXRND1, or both and the stability of the degron reporter was determined by flow cytometry. G. Reductive stress-dependent degradation of the FNIP1 degron reporter requires the degron Cys residues. GFP fused to the wild-type degron (WT) or a degron with all three Cys residues mutated to Ser (CS) was co-expressed with FEM1B, and cells were depleted of glutamine to induce reductive stress, as indicated. The GFP/mCherry ratio was measured as an indication for GFP stability by flow cytometry.

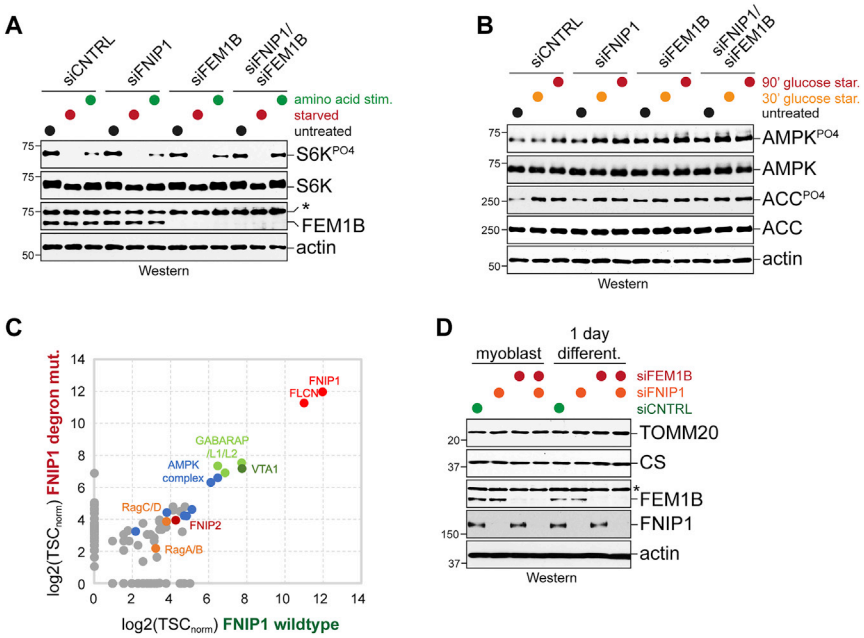

Figure S6. FEM1B and FNIP1 Control Metabolism, Related to Figure 7

A. C2C12 myoblasts were depleted of FEM1B, FNIP1, or both. Cells were starved, before amino acids were added to rapidly turn on mTORC1. mTORC1 activity was monitored by measuring levels of phosphorylated S6 kinase using western blotting. B. C2C12 myoblasts were depleted of FEM1B, FNIP1, or combinations thereof, and AMPK signaling was monitored by measuring phosphorylated ACC and AMPK using western blotting. C. ^{FLAG}FNIP1 or a ^{FLAG}FNIP1^{3CS} degron variant were expressed with ^{HA}FLCN in 293T cells, and binding partners were determined by affinity-purification and mass spectrometry. D. Mitochondrial protein abundance is not altered when FEM1B is depleted. C2C12 myoblasts were transfected with indicated siRNAs and analyzed by western blot for TOMM20 (outer mitochondrial membrane protein) and CS (citrate synthase, matrix).

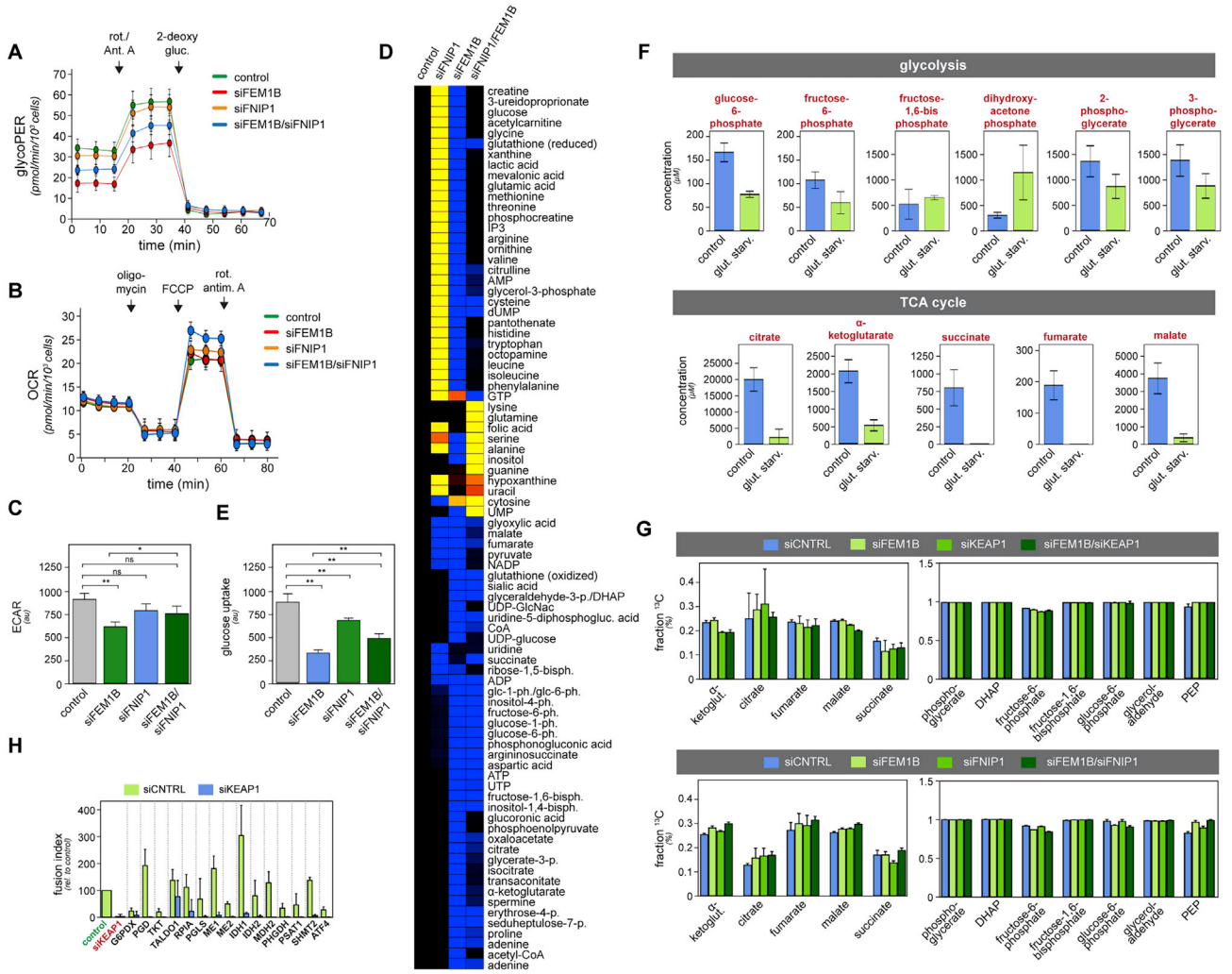

Figure S7. FNIP1 and FEM1B Control the Abundance of Mitochondrial Metabolites and Shuttles, Related to Figure 7

A. C2C12 myoblasts were depleted of FEM1B, FNIP1, or both and the glycolytic rate was determined using a Seahorse Analyzer, showing mean ± SEM B. The oxygen consumption rate (OCR) was measured for C2C12 cells transfected with indicated siRNAs using the mito stress test on a Seahorse Analyzer, showing mean ± SEM C. Depletion of FEM1B reduces the extracellular acidification rate, which is partially rescued by co-depletion of FNIP1, showing mean ± SEM D. C2C12 cells were transfected with siRNAs targeting FNIP1, FEM1B, or both. Polar metabolites were extracted and analyzed by liquid chromatography and mass spectrometry. E. FEM1B depletion inhibits glucose uptake. Standard deviation of four technical replicates normalized to cell number. F. Quantification of glycolytic and TCA cycle metabolites either in untreated control C2C12 myoblasts or C2C12 myoblasts starved for glutamine for 8h. G. C2C12 myoblasts were depleted with indicated siRNAs and labeled with ^{13}C glucose for 4 h. % ^{13}C labeled metabolites were determined by mass spectrometry. H. NRF2 targets in the pentose phosphate pathway, NADPH regeneration and serine biosynthesis do not rescue the KEAP1 depletion phenotype. C2C12 myoblasts were depleted of indicated genes with or without KEAP1 co-depletion and induced to differentiated for 4 days. Myotube formation was monitored by microscopy against MyHC and quantified by automated microscopy. Quantification is of 3 biological replicates, showing mean ± SEM.